ELSEVIER

Contents lists available at ScienceDirect

## **Composite Structures**

journal homepage: www.elsevier.com/locate/compstruct



# A local approach to stress-constrained topology optimization of multi-material structures

Juan P. Giraldo-Isaza<sup>®</sup>, Oliver Giraldo-Londoño<sup>®</sup>

Department of Civil and Environmental Engineering, University of Missouri, Columbia, MO, USA

#### ARTICLE INFO

# Keywords: Stress constraints Yield criterion Multi-material topology optimization Augmented Lagrangian method Additive manufacturing

#### ABSTRACT

Recent advances in multi-material topology optimization and additive manufacturing have enabled the design and fabrication of complex, high-performance structures. However, most existing approaches focus on stiffness maximization and overlook local material failure, which may render non-functional designs that fail under applied loading. Designing functional multi-material structures that can withstand mechanical loads requires accounting for the distinct failure behaviors of each candidate material. This study presents a framework for stress-constrained multi-material topology optimization that incorporates material-specific failure via a unified yield function capable of modeling pressure-independent and pressure-dependent materials, thus capturing the tension-compression strength asymmetry typical of polymers used in multi-material additive manufacturing (e.g., PolyJet 3D printing). Our method explicitly imposes local stress constraints for each material within every finite element, without relying on interpolated failure models. To ensure scalability and robustness, we solve the constrained optimization problem using the augmented Lagrangian method. We demonstrate the effectiveness of our approach through several numerical examples that highlight the benefits of combining materials with tension-compression strength asymmetries to reduce structural mass. Experimental validation of a fabricated design confirms the ability of our approach to predict structural performance and yield limits of multi-material, optimized components.

#### 1. Introduction

Simulation-driven design techniques such as topology optimization are transforming engineering practice by enabling the exploration of complex design spaces and the creation of innovative, organic structures that surpass the capabilities of traditional analytical methods and human intuition. Despite these advances, identifying optimal designs remains a significant challenge, particularly when considering multiple materials with distinct mechanical properties and failure behaviors. While most existing formulations are limited to single-material structures, multi-material topology optimization offers a broader design space by enabling the strategic integration of materials with complementary properties, thereby enhancing mechanical and functional performance. Building on our previous work on stress-constrained topology optimization for lightweight, single-material structures [1], we extend our methodology to address the design of multi-material structures, thus offering greater design flexibility and the potential for substantial performance gains.

In this study, we introduce a multi-material stress-constrained formulation that enforces a broad class of stress constraints through a unified yield function [1]. Based on our previous work [1–3], we employ the augmented Lagrangian (AL) method to solve the optimization problem, ensuring mathematical rigor while accommodating a large number of local stress constraints efficiently. At each optimization iteration, our AL-based framework imposes one local stress constraint per element and candidate material. Although we do not include explicit interfacial stress constraints, this modeling choice is supported by our experimental results on PolyJet-printed specimens, which exhibited no interfacial failure. By incorporating multiple materials with distinct failure criteria, we highlight the potential of exploiting their diverse mechanical properties to achieve lighter, more efficient structures.

The remainder of this paper is organized as follows. Section 2 outlines the motivation for this work and reviews relevant literature in the field. In Section 3, we introduce the multi-material stress-constrained topology optimization problem and discuss the AL-based solution strategy. Section 4 presents several numerical examples that demonstrate the capabilities of the framework, while Section 5 details the printing process, material characterization, and experimental validation of a selected design. Section 6 summarizes the main contributions and implications of this study. Afterward, we present several appendices that

E-mail address: ogiraldo@missouri.edu (O. Giraldo-Londoño).

<sup>\*</sup> Corresponding author.

provide supporting technical details. Appendix A provides details of the sensitivity analysis, Appendix B describes the postprocessing subroutine used to eliminate necking at the interfaces between materials, Appendix C presents convergence plots for all the examples discussed in this work, Appendix D discusses the sensitivity of the framework to selected algorithmic parameters, and Appendix E lists the nomenclature used throughout the paper.

#### 2. Motivation and related work

Since its introduction by Bendsøe and Kikuchi [4], topology optimization has evolved to handle a variety of design problems, including multi-material designs. Multi-material topology optimization has been applied to a wide range of problems, including the design of compliant force inverters [5], composites with tunable thermal expansion [6] or extremal bulk modulus [7], truss structures [8], and optimally graded structures with targeted eigenfrequencies [9]. Despite this progress, existing approaches often lack the ability to incorporate stress constraints explicitly or to address the distinct failure behaviors of multiple materials within a unified framework.

Given the limitations of most existing approaches, there is a critical need for a robust multi-material topology optimization framework that explicitly enforces stress constraints and captures the distinct failure criteria of different candidate materials. Developing such a framework requires addressing several key challenges, including handling a large number of stress constraints, considering multiple failure criteria, and resolving the singularity phenomenon inherent in stress-constrained problems [10,11]. Additionally, the framework must employ effective material interpolation schemes that discourage intermediate densities and prevent material mixing at the end of the optimization iterations.

Multiple material interpolation methods have been developed since Thomsen [12] first studied the topology optimization of structures made of one or two isotropic materials, with the majority of these methods extending the Solid Isotropic Material with Penalization (SIMP) interpolation scheme [8,13-15]. Among these, Discrete Material Optimization (DMO)-based approaches [16-18] have emerged as a particularly effective approach for problems involving many candidate materials. In DMO-based approaches, each design variable corresponds directly to the density of a specific material, providing a direct representation of material distribution. Their simplicity and scalability have made DMO-based interpolation schemes widely adopted in densitybased topology optimization of multi-material structures [8,18-20]. In this work, we adopt the DMO-based interpolation scheme by Sanders et al. [18], which introduces a parameter that controls the extent of penalization of material mixing. This strategy ensures robust convergence and manufacturability, particularly when scaling to a large number of candidate materials.

Beyond the inherent complexities of multi-material topology optimization, incorporating stress constraints into the optimization framework introduces further complexity. Being a local quantity, stress must remain within material-specific limits at any point within the domain to prevent material failure. Enforcing these constraints directly leads to a large number of local constraints, which renders the optimization problem computationally intensive. To reduce the computational cost, many studies have adopted stress aggregation techniques [21–26], which approximate the maximum stress in the design domain using smooth global measures such as the Kreisselmeier-Steinhauser (KS) [27] and the p-norm functions [28]. Although these approaches reduce the number of constraints, the quality of the solutions heavily depends on the approximation parameters, and their effectiveness diminishes as the number of local constraints increases.

An alternative strategy employed in the literature involves using *clustering techniques* [29–31], which aggregate stress over subregions, or clusters, within the domain. This strategy also reduces the number of constraints and improves computational tractability. However, the

quality of the results obtained using these methods is highly sensitive to how the clusters are defined and how many are used.

In contrast to aggregation-based approaches, the augmented Lagrangian (AL) method [32–34] offers a scalable and effective framework for solving topology optimization problems with numerous local constraints. In the AL method, a constrained optimization problem is solved as a sequence of unconstrained problems aimed to minimize the augmented Lagrangian function. This approach provides a robust framework for handling a wide range of optimization problems, including those with degenerate constraints [35,36].

The AL method has been employed to solve stress-constrained topology optimization since the early 2000s. However, early implementations of this method exhibited limitations in robustness and convergence. For instance, Pereira et al. [37] applied the AL method to density-based topology optimization using relaxed stress constraints, but their approach struggled to converge to clear 0/1 designs. Similarly, Emmendoerfer and Fancello [38,39] implemented an AL framework into the level-set topology optimization method to enforce local stress constraints, but their results were sensitive to parameter choices, which limited their general applicability. For a more detailed discussion of the early applications of AL-based approaches to stress-constrained topology optimization, interested readers are referred to Senhora et al. [40].

Recent work has overcome the limitations observed in early applications of the AL method to the stress-constrained problem, with modern formulations yielding robust, mesh-independent solutions [1,2,41]. In particular, these methods achieve stable convergence under mesh refinement and can handle problems with thousands to millions of local stress constraints. The AL method also enables efficient sensitivity analysis using the adjoint method, requiring only a single adjoint vector<sup>1</sup> to be computed at each optimization step—an important advantage for large-scale problems. Senhora et al. [40] demonstrated the efficiency of the AL method by solving static problems with over one million local stress constraints in a few hours on a standard desktop computer. Building on this, Giraldo-Londoño and Paulino [2] demonstrated that the computational cost of the AL method is comparable to that of a standard compliance minimization problem, with the primary overhead arising from the computation of the adjoint vector. Extending the method further, Giraldo-Londoño et al. [42] applied the AL framework to transient dynamic problems, demonstrating its ability to handle more than 200 million constraints. Collectively, these studies highlight the potential of the AL method as a powerful and scalable approach for practical engineering design.

Beyond the challenge of handling a large number of stress constraints, another major challenge in stress-constrained topology optimization is the stress singularity phenomenon. This issue was first reported by Sved and Ginos [10] and later by Kirsch [43] when dealing with truss optimization under stress constraints. The singularity phenomenon arises when the optimal solution lies in a lower-dimensional, degenerate region of the design space that standard optimization methods cannot access, often leading to suboptimal designs. This problem has been addressed using two main strategies: constraint relaxation techniques [37,44–46] and vanishing constraints [46].

Constraint relaxation techniques address the singularity problem by softening the stress constraints (e.g., as in the  $\varepsilon$ -relaxation approach by Cheng and Guo [44], where a constraint of the form  $g(\mathbf{z}) \leq 0$  is converted into a constraint of the form  $g(\mathbf{z}) \leq \varepsilon$ ). Although effective, constraint relaxation techniques alter the shape of the design space and may yield infeasible solutions that violate the original, unrelaxed constraints. In contrast, the vanishing constraint approach preserves the shape of the feasible domain by introducing constraints that *vanish* 

 $<sup>^{1}</sup>$  This is valid only for linear and nonlinear elastic systems with a single load case. For example, multiple load cases require the solution of multiple adjoint problems, as shown in Appendix A.

Table 1
Comparison between stress-constrained multi-material topology optimization formulations.

Approach	Representative works	Multi-material handling	Validation	Observations
Global (e.g., p-norm)	Jeong et al. [47], Chu et al. [55], Chu et al. [48], Xu et al. [49], Chen et al. [52], Liao et al. [56], Yaghoobi et al. [57]	Single yield criterion (von Mises)	Numerical only	Loses control over local nature of stress and quality of solutions are parameter dependent
Local (e.g., AL method)	Kundu et al. [53], Kundu and Zhang [58], Ding et al. [54], Kundu and Zhang [59]	Distinct yield criteria (e.g., von Mises, Drucker–Prager, Tsai–Wu) with yield criteria interpolation	Mostly numerical, with one showing experimental results [58]	Yield function interpolation adds nonlinearities and results depend on parameter tuning
This work	-	Distinct yield criteria, without yield function interpolation	Numerical and experimental	Overcomes limitations of interpolation approaches

(i.e., become zero) as the corresponding element density approaches zero, thus avoiding explicit constraint relaxation [40]. Building on the linear vanishing constraint by Cheng and Jiang [46], Giraldo-Londoño and Paulino [1] introduced a *polynomial vanishing constraint* that has proven effective when solving topology optimization problems with local stress constraints. The polynomial vanishing constraint has been successfully employed in the topology optimization of structures made from pressure-independent or pressure-dependent materials [1], structures under general dynamic loading [42], structures constrained by the first principal stress [3], and structures made of nonlinear materials [2].

While significant progress has been made for single-material structures, stress-constrained multi-material topology optimization remains less mature. Most existing approaches approximate material failure using interpolated stress measures, typically based on the von Mises criterion. For example, Jeong et al. [47] introduced the Separable Stress Interpolation (SSI) scheme to apply von Mises stress constraints in multi-material designs, while Chu et al. [48] extended this concept within the level-set framework. Other studies have adopted global *p*-norm stress measures based on the von Mises stress to solve optimization problems involving mass minimization [49], compliance minimization [50], stress minimization under mass constraints [51], and volume minimization under thermomechanical loads and stress constraints [52].

However, the von Mises criterion is not suitable for materials that exhibit tension-compression strength asymmetry or sensitivity to hydrostatic pressure, such as concrete, polymers, and foams, as well as the polymeric materials commonly used in multi-material additive manufacturing. In the context of single-material topology optimization, Giraldo-Londoño and Paulino [1] addressed this limitation by introducing a unified yield criterion capable of reproducing several classical pressure-independent and pressure-dependent yield criteria, including von Mises, Drucker-Prager, Tresca, Mohr-Coulomb, Bresler-Pister, and Willam-Warnke. Kundu et al. [53] later extended this concept to stress-constrained multi-material topology optimization and used a SIMP-like yield function interpolation scheme to enforce stress constraints across different materials. While promising, a key limitation of this approach is that the interpolated yield surfaces at intermediate densities lack physical meaning and may overestimate material strength unless the interpolation parameters are carefully tuned. A similar issue arises in the work of Ding et al. [54], who proposed a scalar unified Stress Yield Factor (SYF) that combines the von Mises and Drucker-Prager criteria into a single, interpolated yield function per element. Although effective for that specific combination of yield criteria, the SYF approach does not generalize easily to other yield functions and introduces additional parameters that influence the interpolation behavior.

An overview of existing studies on stress-constrained multi-material topology optimization is provided in Table 1. Among the studies listed in the table, only a limited number of them explicitly consider distinct yield criteria [53,54,59]. Despite differences in their formulations, these methods rely on nonlinear interpolation of yield functions to

combine multiple material failure behaviors into a single, approximate criterion, which introduces additional assumptions and complexity. While these strategies reduce the number of constraints per element from m to one, where m is the number of candidate materials, they introduce approximate, non-physical yield surface representations, particularly during early optimization stages when intermediate densities and material mixing are common. These methods also require parameter tuning to prevent strength overestimation when material mixing is present, and add further nonlinearities to an already highly nonlinear optimization problem, increasing the likelihood of producing suboptimal solutions.

To address the challenges discussed above, this study adopts a local formulation that assigns one stress constraint per element and per candidate material, eliminating the need to interpolate between yield criteria. Each material retains its own failure criterion, ensuring strict enforcement of stress constraints throughout the optimization process and enabling clear material separation based on local strength demands. This approach does not require tuning yield surface interpolation parameters and directly avoids strength overestimation by enforcing each material failure criterion separately. Although our approach requires imposing a larger number of stress constraints because it requires enforcing m constraints per element instead of one, the overall computational cost remains comparable to that of problems in which yield criteria interpolation is used, as the augmented Lagrangian method efficiently handles the expanded constraint set. Notably, despite enforcing one stress constraint per element and per candidate material, the sensitivity analysis still requires only a single adjoint vector, just as in the single-material case [1,2]. Importantly, our study is among the first to experimentally assess the performance of multi-material structures designed through stress-constrained topology optimization, offering direct evidence of structural performance and demonstrating the practical viability of the proposed framework.

## 3. Problem formulation and methodology

This section discusses the formulation of the stress-constrained multi-material topology optimization problem introduced in this study and the associated AL-based solution strategy. We begin by defining the optimization problem, which seeks to minimize a weighted mass objective while enforcing one stress constraint per element and candidate material. We then provide details of the unified yield criterion by Giraldo-Londoño and Paulino [1], which we use to characterize the failure behavior of each candidate material. Finally, we outline the AL-based strategy employed to solve the stress-constrained topology optimization problem efficiently.

## 3.1. Multi-material stress-constrained formulation

Our formulation aims to find the lightest structure capable of withstanding applied loads without failing locally at any point within the domain. We prevent material failure by imposing local stress constraints,  $g_{\ell i}$ , at the centroid of each finite element,  $\ell=1,\ldots,N$ , in the domain, and for each candidate material,  $i=1,\ldots,m$ . The optimization problem is formulated as follows:

$$\min_{\mathbf{z} \in [0,1]^{N \times m}} f(\mathbf{z}) = \frac{\sum_{i=1}^{m} \gamma_i \mathbf{A}^T \mathbf{V}_i}{\sum_{i=1}^{m} \gamma_i \mathbf{A}^T \mathbf{1}}$$
s.t.  $g_{\ell i}(\mathbf{z}, \mathbf{u}) \le 0$ ,  $\ell = 1, \dots, N$ ;  $i = 1, \dots, m$  (1)

Here,  $f(\mathbf{z})$  represents a weighted mass ratio, expressed in terms of the design variable matrix,  $\mathbf{z} = \{z_{\ell 1}, \dots, z_{\ell m}\}_{\ell=1}^N$ . Each design variable,  $z_{\ell i} \in [0,1]$ , indicates the presence of material i in element  $\ell$ . The parameter  $\gamma_i$  is a material-specific weight factor, which may correspond to properties such as mass density or material cost. The vector  $\mathbf{A} = \{|\Omega_\ell|\}_{\ell=1}^N$  contains the area (in 2D) or volume (in 3D) of each finite element, while  $\mathbf{V}_i = m_V(\mathbf{y}_i)$  represents the vector of volume fractions for candidate material i, computed via the threshold projection function [60]:

$$m_{V}\left(y_{\ell i}\right) = \frac{\tanh(\bar{\beta}\bar{\eta}) + \tanh\left(\bar{\beta}\left(y_{\ell i} - \bar{\eta}\right)\right)}{\tanh(\bar{\beta}\bar{\eta}) + \tanh(\bar{\beta}(1 - \bar{\eta}))},\tag{2}$$

where parameters  $\bar{\beta}$  and  $\bar{\eta}$  control the aggressiveness and cutoff density of the projection (see Appendix D.2), respectively, and  $\mathbf{y}_i \left( \mathbf{z}_i \right) = \mathbf{P}\mathbf{z}_i$  is the vector of filtered densities for candidate material i, computed using the polynomial filter [61]:

$$P_{ij} = \frac{w_{ij}A_j}{\sum_{k=1}^{N} w_{ik}A_k}, \text{ with } w_{ij} = \max \left[0, 1 - \frac{\|\mathbf{x}_i - \mathbf{x}_j\|_2}{R}\right]^q,$$
 (3)

where  $\|\mathbf{x}_i - \mathbf{x}_j\|_2$  is the Euclidean distance between the centroids of elements i and j, R is the filter radius, and q is the filter exponent.

The displacement field,  $\mathbf{u}$ , is obtained by solving the linear equilibrium equation  $K\mathbf{u} = F$ , where K is the global stiffness matrix and F is the global load vector. The stiffness matrix is assembled from element contributions as:

$$\mathbf{K} = \sum_{\ell=1}^{N} \mathbf{k}_{\ell}, \text{ with } \mathbf{k}_{\ell} = \sum_{i=1}^{m} W_{\ell i} \mathbf{k}_{\ell i} \text{ and } \mathbf{k}_{\ell i} = \int_{\Omega_{\ell}} \mathbf{B}_{\ell}^{T} \mathbf{D}_{0i} \mathbf{B}_{\ell} d\mathbf{x}. \tag{4}$$

Here,  $\sum_{\ell=1}^N$  denotes the standard finite element (FE) assembly operator. For each element  $\ell$ ,  $\mathbf{k}_{\ell i}$  represents the stiffness matrix when the element is filled entirely with material i, where  $\mathbf{B}_{\ell}$  is the strain-displacement matrix,  $\mathbf{D}_{0i}$  is the material moduli matrix of candidate material i, and  $\Omega_{\ell}$  is the domain occupied by the element. The effective stiffness matrix,  $\mathbf{k}_{\ell}$ , is then computed as a weighted sum of the material stiffness matrices  $\mathbf{k}_{\ell i}$ , with weights  $W_{\ell i} = m_W\left(E_{\ell i}\right)$  obtained from the modified Discrete Material Optimization (DMO) interpolation function [181].

$$m_W\left(E_{\ell i}\right) = E_{\ell i} \prod_{\substack{j=1\\j \neq i}}^{m} \left(1 - \tau E_{\ell j}\right),\tag{5}$$

where  $E_{\ell i}$  are the penalized densities for element  $\ell$  and material i, and  $\tau \in [0,1]$  is a mixing penalty factor that controls the extent of penalization of material mixing. For instance, a value of  $\tau = 0$  imposes no penalization, allowing material mixing, while a value of  $\tau = 1$  fully penalizes material mixing, promoting distinct material phases.

The penalized densities,  $E_{\ell i}=m_E\left(V_{\ell i}\right)$ , are computed using the SIMP interpolation function,

$$m_E\left(V_{\ell i}\right) = \varepsilon + (1 - \varepsilon)V_{\ell i}^p,\tag{6}$$

where p is the penalization power and  $\varepsilon \ll 1$  is an Ersatz parameter used to prevent numerical singularities when  $V_{\ell i} \to 0$ . With these variable transformations defined, Algorithm 1 summarizes the global stiffness matrix computation in a concise step-by-step form.

Fig. 1 illustrates the behavior of the modified DMO interpolation function used to compute the interpolated stiffness matrix. For Algorithm 1 Step-by-step computation of the global stiffness matrix

Step 1. Compute filtered densities (Eq. (3)):

$$y_{\ell i} = \sum_{i=1}^{N} P_{\ell j} z_{ji}$$

Step 2. Obtain the projected (physical) densities (Eq. (2)):

$$V_{\ell i} = m_V(y_{\ell i}).$$

Step 3. Evaluate the penalized densities (Eq. (6)):

$$E_{\ell i} = m_E(V_{\ell i}).$$

**Step 4.** Evaluate the element-wise material weights using the modified DMO interpolation function (Eq. (5)):

$$W_{\ell i} = m_W(E_{\ell i}).$$

**Step 5.** Obtain the effective stiffness matrix of element  $\ell$  and assemble the global stiffness matrix (Eq. (4)):

$$\mathbf{k}_{\ell} = \sum_{i=1}^{m} W_{\ell i} \, \mathbf{k}_{\ell i}, \qquad \mathbf{K} = \sum_{\ell=1}^{N} \mathbf{k}_{\ell}.$$

demonstration purposes, we consider a simplified case in which the DMO function is used to compute the effective Young's modulus of an element  $\ell$  when considering two candidate materials with Young's moduli  $Y_i^0 = 1$ , i = 1, 2. The effective Young's modulus is given by  $Y_{\ell} = \sum_{i=1}^{2^{-1}} W_{\ell i} Y_i^0$ . Figs. 1a-c illustrate how the interpolation function evolves as  $\tau$  and p vary. In Fig. 1a, for  $\tau = 0$  and p = 1, the interpolation reduces to a linear combination of the individual Young's moduli. Because material mixing is not penalized in this case (i.e.,  $\tau = 0$ ), the topology optimization results would produce intermediate density values and mixed-material regions. As shown in Fig. 1b, increasing  $\tau$  and p progressively reduces the efficiency of intermediate densities and material mixing.<sup>2</sup> Specifically, p > 1 penalizes intermediate values of  $V_{\ell i}$  (analogously to the single-material SIMP interpolation), while  $\tau \in (0,1]$  penalizes material mixing (i.e., having  $V_{\ell 1}$  and  $V_{\ell 2}$  be simultaneously nonzero becomes less efficient as  $\tau$  increases). In the limiting case shown in Fig. 1c, when  $\tau = 1$ , the interpolated modulus drops to zero if both penalized densities are equal to one, and the maximum stiffness is achieved only when one material density equals one and the other equals zero. Hence, p > 1 discourages intermediate density values, while  $\tau = 1$  strongly discourages material mixing, promoting discrete zero–one solutions without  $V_{\ell 1}$  and  $V_{\ell 2}$  being simultaneously equal to one within a given element.

#### 3.2. Stress constraint definition

As previously discussed, our formulation prevents material failure by enforcing local stress constraints on each element  $\ell$  and candidate material i. In this study, we adopt the polynomial vanishing constraint introduced by Giraldo-Londoño and Paulino [1], which extends the traditional linear vanishing constraint [46] by including a cubic term that penalizes constraint violation more severely. The cubic term drives the solution to a density distribution with overall lower stresses [2] compared with the linear vanishing constraint. The polynomial vanishing constraint is defined as:

$$g_{\ell i}(\mathbf{z}, \mathbf{u}) = E_{\ell i} \Lambda_{\ell i} \left( \Lambda_{\ell i}^2 + 1 \right) \le 0, \quad \ell = 1, \dots, N; \ i = 1, \dots, m, \tag{7}$$

 $<sup>^2</sup>$  In the context of this example, material mixing occurs when both  $V_{\ell 1}$  and  $V_{\ell 2}$  are simultaneously nonzero.

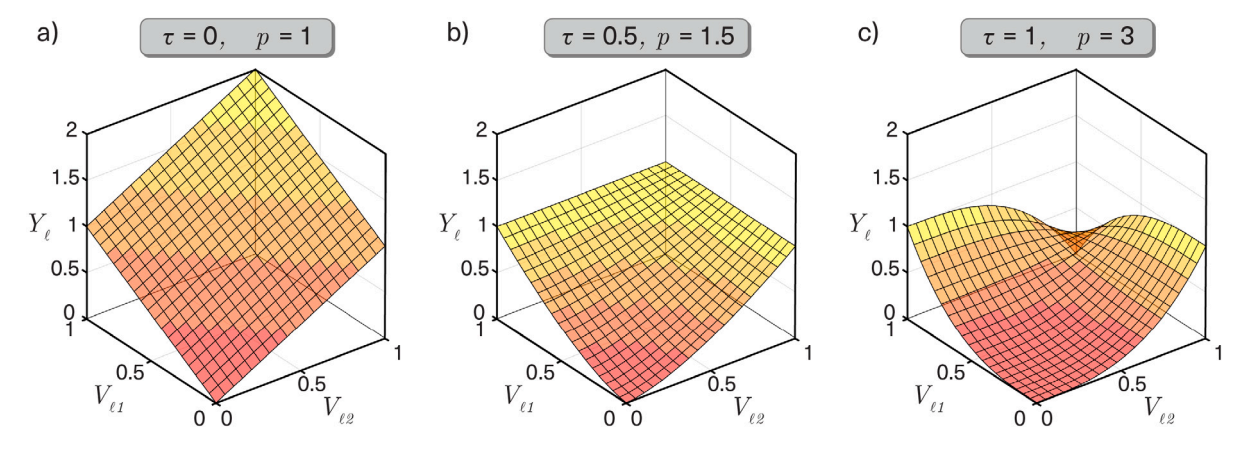


**Fig. 1.** Influence of penalization parameters  $\tau$  and p on the Young's modulus interpolation  $Y_{\ell}$  for 2 candidate materials. Panels correspond to (a)  $\tau = 0$ , p = 1; (b)  $\tau = 0.5$ , p = 1.5; (c)  $\tau = 1$ , p = 3.

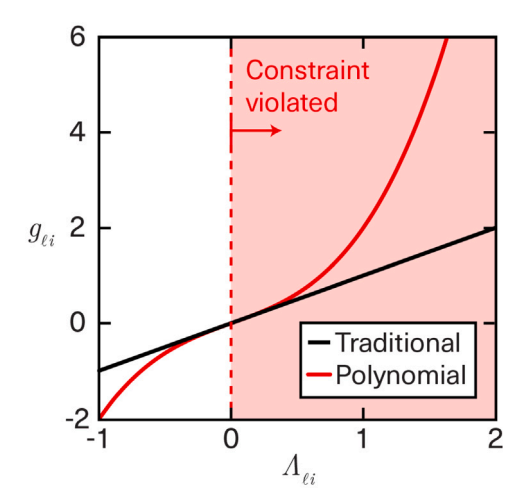


**Fig. 2.** Comparison between the traditional vanishing constraint [46] and the polynomial vanishing constraint [1] as a function of  $\Lambda_{\ell i}$ . Values of  $\Lambda_{\ell i} > 0$  indicate stress constraint violation.

where  $E_{\ell i}$  are the penalized densities and  $\Lambda_{\ell i}$  is a unified criterion that characterizes the failure behavior within element  $\ell$  for candidate material i. By including  $E_{\ell i}$ , the constraint naturally vanishes as the material density approaches zero, thereby avoiding stress singularities in void regions. Fig. 2 provides a graphical representation of the polynomial vanishing constraint and compares it with the traditional linear vanishing constraint by Cheng and Jiang [46].

The unified failure function,  $\Lambda_{\ell i}$ , is defined as:

$$\Lambda_{\ell i} = \sigma_{\ell i}^{eq} - 1,\tag{8}$$

where  $\sigma^{eq}_{\ell i}$  is a dimensionless equivalent stress measure that generalizes multiple classical yield criteria. The equivalent stress measure is given by:

$$\sigma_{\ell_i}^{eq} = \hat{\alpha}(\theta)\sqrt{3J_2} + \hat{\beta}I_1 + \hat{\gamma}I_1^2,\tag{9}$$

where  $I_1$  is the first invariant of the Cauchy stress tensor,  $\sigma_{\ell i}$ , and  $J_2$  is the second invariant of the deviatoric stress tensor,  $\mathbf{s}_{\ell i}$ . The scalar terms  $\hat{\alpha}(\theta)$ ,  $\hat{\beta}$ , and  $\hat{\gamma}$  define the shape of the yield surface and are chosen to match specific failure criteria [1].

The stress invariants are computed as:

$$I_1 = \overline{\mathbf{M}} \sigma_{\ell i} \tag{10}$$

and

$$J_2 = \frac{1}{3} \sigma_{\ell i}^T \overline{\mathbf{V}} \sigma_{\ell i},\tag{11}$$

where  $\overline{\mathbf{M}} = [1 \ 1 \ 0]$  and  $\sigma_{\ell i} = [\sigma_{11} \ \sigma_{22} \ \sigma_{12}]^T$  for 2D problems, and  $\overline{\mathbf{M}} = [1 \ 1 \ 1 \ 0 \ 0]$  and  $\underline{\sigma}_{\ell i} = [\sigma_{11} \ \sigma_{22} \ \sigma_{33} \ \sigma_{23} \ \sigma_{13} \ \sigma_{12}]^T$  for 3D problems. Likewise, the matrix  $\overline{\mathbf{V}}$  used to evaluate the second invariant of the deviatoric stress tensor is given by

$$\overline{\mathbf{V}} = \begin{bmatrix} 1 & -1/2 & 0 \\ -1/2 & 1 & 0 \\ 0 & 0 & 3 \end{bmatrix}$$
 (12)

for 2D problems and

$$\overline{\mathbf{V}} = \begin{bmatrix} 1 & -1/2 & -1/2 & 0 & 0 & 0 \\ -1/2 & 1 & -1/2 & 0 & 0 & 0 \\ -1/2 & -1/2 & 1 & 0 & 0 & 0 \\ 0 & 0 & 0 & 3 & 0 & 0 \\ 0 & 0 & 0 & 0 & 3 & 0 \\ 0 & 0 & 0 & 0 & 0 & 3 \end{bmatrix}$$
 (13)

for 3D problems.

The Cauchy stress vector for candidate material i is evaluated at the centroid of element  $\ell$  as:

$$\sigma_{\ell i} = \mathbf{D}_{0i} \mathbf{B}_{\ell} \mathbf{u}_{\ell},\tag{14}$$

where  $\mathbf{D}_{0i}$  is the material moduli matrix of candidate material i,  $\mathbf{B}_{\ell}$  is the strain displacement matrix at the centroid of element  $\ell$ , and  $\mathbf{u}_{\ell}$  is the displacement vector of element  $\ell$ .

The term  $\hat{a}(\theta)$  in Eq. (9) is referred to as the deviatoric function [1], and it defines the shape of the yield surface when intersected by the deviatoric plane. The deviatoric function is given by

$$\hat{\alpha}(\theta) = \frac{A\cos^2\hat{\theta} + B}{C\cos\hat{\theta} + \sqrt{D\cos^2\hat{\theta} + E}},\tag{15}$$

where

$$\hat{\theta} = \frac{1}{3}\sin^{-1}[\zeta\sin 3\theta] + \bar{\theta}, \quad \zeta \le 1,$$
(16)

and

$$\theta = \frac{1}{3}\sin^{-1}\left(-\frac{3\sqrt{3}}{2}\frac{J_3}{J_2^{3/2}}\right), \quad -\frac{\pi}{6} \le \theta \le \frac{\pi}{6},\tag{17}$$

is the Lode angle [62], which is a function of the third invariant of the deviatoric stress tensor given by

$$J_3 = \frac{1}{3}I_1\left(J_2 - \frac{1}{9}I_1^2\right) \tag{18}$$

for 2D problems and by

$$J_3 = s_{11}s_{22}s_{33} + 2\sigma_{23}\sigma_{13}\sigma_{12} - \left(s_{11}\sigma_{23}^2 + s_{22}\sigma_{13}^2 + s_{33}\sigma_{12}^2\right) \tag{19}$$

for 3D problems, where  $s_{uv}$ , u, v = 1, ..., 3 are the components of the deviatoric stress tensor,

$$\mathbf{s}_{\ell i} = \sigma_{\ell i} - \frac{I_1}{3} \overline{\mathbf{M}}^T. \tag{20}$$

**Table 2** Parameters defining the unified equivalent stress measure.

Failure criterion	$\hat{lpha}( heta)$								
	$\overline{A}$	В	С	D	E	ζ	$\bar{\theta}$	$\hat{eta}$	Ŷ
von Mises <sup>a</sup>	0	1	0	0	1	1	0	0	0
Drucker–Prager <sup>b</sup>	0	$\frac{\sigma_{lim}}{\sigma_c + \sigma_t}$ $\frac{\sigma_c + \sigma_t}{2\sigma_c \sigma_t}$	0	0	1	1	0	$\frac{\sigma_c - \sigma_t}{2\sigma_c \sigma_t}$ $\frac{\sigma_b - \sigma_t}{\sigma_b}$	0
Willam–Warnke <sup>c</sup>	$A_W$	$B_W$	$C_W$	$D_W$	$E_W$	1	$\frac{\pi}{6}$	$\frac{\sigma_b - \sigma_t}{3\sigma_b\sigma_t}$	0
Mohr-Coulomb <sup>d</sup>	$A_{MC}$	0	1	0	0	≤ 1	$ec{ ilde{ heta}}$	$\frac{\sigma_c - \sigma_t}{3\sigma_c \sigma_t}$	0

(21)

<sup>d</sup> 
$$A_{MC} = (2\alpha/3)\sqrt{3 + (\beta/\alpha)^2}$$
 and  $\tan \tilde{\theta} = \frac{\beta}{\alpha\sqrt{3}}$  where  $\alpha = \frac{\sigma_c + \sigma_t}{2\sigma_c \sigma_t}$  and  $\beta = \frac{\sigma_c - \sigma_t}{2\sigma_c \sigma_t}$ .

As shown by Giraldo-Londoño and Paulino [1], a suitable choice of parameters A-E,  $\zeta$ ,  $\bar{\theta}$ ,  $\hat{\beta}$ , and  $\hat{\gamma}$ , conducts to the representation of several classical yield criteria including von Mises, Drucker–Prager, Willam–Warnke, and Mohr–Coulomb. Table 2 presents the parameters used to generate the yield surfaces for the various criteria employed in this study. The parameters for the Willam–Warnke yield criterion used in Section 5 are defined as  $A=A_W$ ,  $B=B_W$ ,  $C=C_W$ ,  $D=D_W$ ,  $E=E_W$ , which are given by

$$\begin{split} A_{\mathrm{W}} &= \frac{4}{\sigma_c} \sqrt{\frac{2}{15}} \left( r_c^2 - r_t^2 \right), \quad B_{\mathrm{W}} = \frac{1}{\sigma_c} \sqrt{\frac{2}{15}} \left( r_c - 2 r_t \right)^2, \quad C_{\mathrm{W}} = 2 r_c \left( r_c^2 - r_t^2 \right), \\ D_{\mathrm{W}} &= 4 r_c^2 \left( r_c - 2 r_t \right)^2 \left( r_c^2 - r_t^2 \right), \quad E_{\mathrm{W}} = r_c^2 \left( r_c - 2 r_t \right)^2 \left( 5 r_t^2 - 4 r_t r_c \right), \end{split}$$

where

$$r_c = \sqrt{\frac{6}{5}} \frac{\sigma_b \sigma_t}{3\sigma_b \sigma_t + \sigma_c \left(\sigma_b - \sigma_t\right)} \quad \text{and} \quad r_t = \sqrt{\frac{6}{5}} \frac{\sigma_b \sigma_t}{\sigma_c \left(2\sigma_b + \sigma_t\right)}, \tag{22}$$

with  $\sigma_c$  and  $\sigma_t$  representing the yield stress in uniaxial compression and uniaxial tension, respectively, and  $\sigma_b$  denoting the yield stress in equibiaxial compression. This formulation expands the design space for multimaterial structures by exploiting the distinct mechanical responses of different materials. For instance, it could allow the combination of pressure-dependent materials with high compressive strength and ductile materials with high tensile strength.

For the Mohr–Coulomb yield criterion, the rounding parameter  $\zeta \leq 1$  enables the unified yield function to produce a smooth approximation of the yield surface [63], thereby avoiding numerical issues from gradient discontinuities during topology optimization. Interested readers are referred to the work of Giraldo-Londoño and Paulino [1] for a detailed discussion of the unified yield function and its parameters.

Although we enforce element-wise stress constraints per material, we do not include explicit interfacial stress constraints in our formulation. This choice is supported by our experimental validation using PolyJet-printed specimens (see Section 5), which showed no interfacial failure due to the highly integrated material transitions inherent to this printing process [64,65]. Moreover, by enforcing stress constraints directly on each material within every element, the proposed framework avoids key drawbacks of yield-function interpolation schemes—namely, the introduction of additional nonlinearities into an already highly nonlinear problem and the reliance on blending parameters that, if not carefully tuned, may overestimate yield strength and lead to premature failure of the resulting designs.

## 3.3. Solution via the augmented Lagrangian method

Following our previous work [2,3], we solve the optimization problem (1) using an AL-based approach [32–34]. Using this approach, we solve (1) as a sequence of unconstrained minimization problems<sup>3</sup> whose

solutions converge to that of the original optimization problem with local constraints. Specifically, at each step k of the AL method, we solve the following minimization sub-problem:

$$\min_{\mathbf{z} \in [0,1]^{N \times m}} \quad J^{(k)}(\mathbf{z}, \mathbf{u}) = f(\mathbf{z}) + \frac{1}{mN} \sum_{i=1}^{m} \sum_{\ell=1}^{N} \left[ \lambda_{\ell i}^{(k)} h_{\ell i}(\mathbf{z}, \mathbf{u}) + \frac{\mu^{(k)}}{2} h_{\ell i}^{2}(\mathbf{z}, \mathbf{u}) \right],$$

$$k = 0, 1, 2, \dots$$

(23)

where  $J^{(k)}(\mathbf{z},\mathbf{u})$  is the normalized AL function [2], which consists of the objective function  $f(\mathbf{z})$  from (1) and a penalization term defined in terms of Lagrange multiplier estimators,  $\lambda^{(k)}_{\ell i}$ , a quadratic penalty factor,  $\mu^{(k)}$ , and equivalent equality constraints,  $h_{\ell i}(\mathbf{z},\mathbf{u})$ , given by:

$$h_{\ell i}(\mathbf{z}, \mathbf{u}) = \max \left( g_{\ell i}(\mathbf{z}, \mathbf{u}), \frac{-\lambda_{\ell i}^{(k)}}{\mu^{(k)}} \right), \tag{24}$$

where  $g_{\ell i}(\mathbf{z}, \mathbf{u})$  are the stress constraints defined in (7). After solving each AL sub-problem, both  $\lambda_{\ell i}^{(k)}$  and  $\mu^{(k)}$  are updated as follows:

$$\lambda_{\ell_i}^{(k+1)} = \lambda_{\ell_i}^{(k)} + \mu^{(k)} h_{\ell_i}(\mathbf{z}^{(k)}, \mathbf{u})$$
 (25)

$$\mu^{(k+1)} = \min\left(\tilde{\alpha}\mu^{(k)}, \mu_{\text{max}}\right),\tag{26}$$

where  $\tilde{a} > 1$  controls the quadratic penalty factor update rate and  $\mu_{\rm max}$  is an upper bound used to prevent ill-conditioning.

The term mN in (23) is used to normalize the penalty term in the AL function, preventing it from growing unbounded as the number of stress constraints increases. This normalization improves numerical stability and has been shown to produce nearly mesh-independent designs, even for problems involving hundreds of thousands of stress constraints (e.g., see [2]). We have successfully applied this normalization strategy to a broad range of stress-constrained problems with applications spanning linear and nonlinear elasticity [2,3,40], dynamics [42], and various yield criteria [1].

To solve the AL sub-problems (23) efficiently using gradient-based optimization algorithms, we need to compute the sensitivities of the augmented Lagrangian function  $J^{(k)}$  with respect to the design variables z. These sensitivities are derived in detail in Appendix A.

Fig. 3 presents a schematic flowchart of our AL-based multi-material topology optimization framework. The process begins with input data related to the finite element problem and the optimizer, and with initialization of  $\lambda_{\ell i}^{(k)}$  and  $\mu^{(k)}$ , for k=0. With these inputs, we then use the method of moving asymptotes (MMA) [66] to approximately solve the AL sub-problem defined in (23). After obtaining an approximate solution, we update the Lagrange multiplier estimators and quadratic penalty factors via Eqs. (25) and (26). This cycle repeats until convergence.

Convergence is achieved when the relative change in design variables satisfies  $\frac{1}{mN}\sum_{\ell=1}^{\infty}\left|\mathbf{z}_{i+1}^{(k)}-\mathbf{z}_{i}^{(k)}\right|<\text{Tol},$  and the maximum normalized equivalent stress,  $\tilde{\sigma}_{\ell i}^{eq}=E_{\ell i}\sigma_{\ell i}^{eq}$ , remains within the prescribed tolerance, i.e.,  $\max(\tilde{\sigma}_{\ell i}^{eq})<1+\text{TolS}.$  Here,  $E_{\ell i}=m_E(V_{\ell i})$  is defined in Eq. (6), Tol

<sup>&</sup>lt;sup>a</sup>  $\sigma_{lim}$  denotes the von Mises yield stress.

b  $\sigma_c$  and  $\sigma_t$  denote the yield stress in uniaxial compression and uniaxial tension, respectively.

 $<sup>^{\</sup>rm c}$   $\sigma_{\rm b}$  denotes yield stress in equibiaxial compression.

<sup>&</sup>lt;sup>3</sup> Although we refer to the AL sub-problems as *unconstrained*, they in fact contain box constraints on the design variables  $(z_{e_i} \in [0,1])$ , as shown in (23).

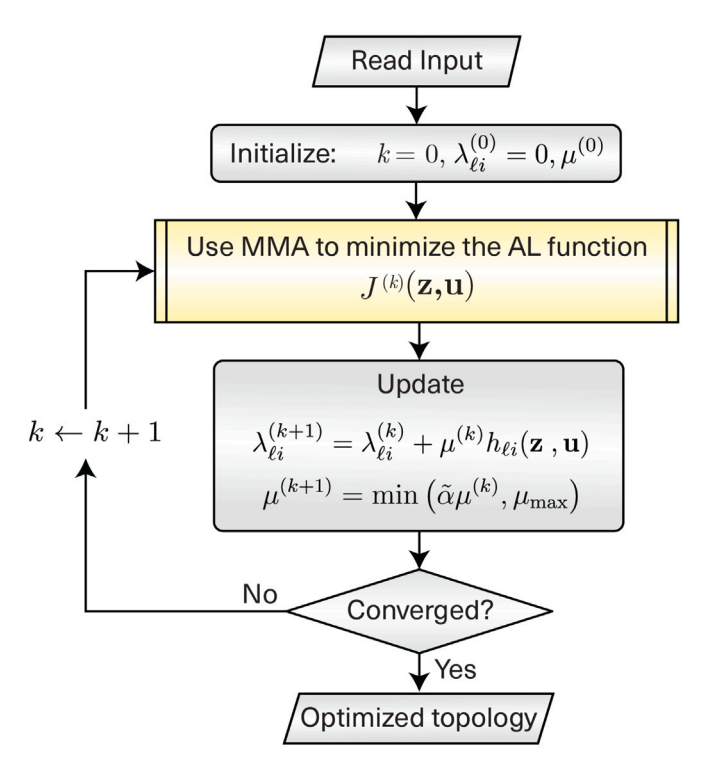


**Fig. 3.** Schematic flowchart of the AL-based topology optimization framework we employ to solve the multi-material topology optimization problem with local stress constraints.

and To1S are user-defined tolerances for the design variable change and the stress constraints, respectively, and  $\mathbf{z}_i^{(k)}$  and  $\mathbf{z}_{i+1}^{(k)}$  denote the design variable matrices at two successive MMA iterations within AL sub-problem k.

To account for multiple load cases, the AL formulation must be extended accordingly. Specifically, each additional load case introduces mN new stress constraints, resulting in a total of  $N_c = mnN$  stress constraints for n load cases. The AL function must be expanded to include a separate set of Lagrange multiplier estimators,  $\lambda_{\ell i}^{(c)}$ , and quadratic penalty terms,  $\frac{\mu}{2}h_{\ell i}^{(c)^2}$ , for each element  $\ell$ , material i, and load case c. Additionally, because each load case contributes its own set of equilibrium equations in (1), the sensitivity analysis requires solving a separate adjoint problem for each load case. Complete details of this formulation and sensitivity derivations are provided in Appendix A.

## 4. Numerical examples

This section presents two numerical examples that demonstrate the capabilities of the proposed framework in designing multi-material structures with various yield criteria. To ensure the reproducibility of the results, Table 3 provides the input parameters used to solve all the problems discussed next. All results were obtained using a Matlab implementation of the formulation discussed previously. First, we discuss the design of a three-dimensional corbel and highlight the benefits of stress-constrained multi-material topology optimization, in which lighter structures can be obtained by the combination of two materials with different yield criteria. Next, we discuss the design of an airless tire composed of three different materials and subjected to multiple load cases, including normal and shear tractions used to simulate ground contact forces as the tire rotates. For clarity and ease of comparison among the optimized designs discussed next, we report the multi-material volume fraction VF rather than the weighted mass

**Table 3** Input parameters used to solve all examples.

Parameter	Value
Initial Lagrange multiplier estimators, $\lambda_{e_i}^{(0)}$	0
Initial penalty factor, $\mu^{(0)}$	10
Maximum penalty factor, $\mu_{max}$	10,000
Penalty factor update parameter, $\tilde{\alpha}$	1.1
SIMP penalization factor, p	3.5
Nonlinear filter exponent, q	3
Ersatz parameter, $\epsilon$	$10^{-8}$
MMA iterations per AL step, MMA_Iter <sup>a</sup>	5
MMA move limit, move	0.15
Initial threshold projection factor, $\bar{\rho}^{\rm b}$	1
Threshold projection factor increment, $\bar{\beta}_{inc}^{b}$	1
Threshold projection factor frequency, $\bar{\rho}_{\text{freq}}^{\ \ b}$	5
Maximum threshold projection factor, $\bar{\beta}_{\max}^{b}$	10
Threshold projection density, $\bar{\eta}$	0.5
Mixing penalty factor, $\tau$	1
Initial guess, $z_{\ell i}^{(0)}$	0.5
Convergence tolerance on design variables, Tol	0.002
Convergence tolerance on stress constraints, TolS	0.003
Maximum number of AL steps, MaxIter	100

<sup>&</sup>lt;sup>a</sup> In practice, the AL function is approximately minimized by performing a limited number of MMA iterations at each AL step. In this study, we employ 5 MMA iterations per AL step [1,2].

ratio  $f(\mathbf{z})$  in (1),

$$VF = \frac{\sum_{i=1}^{m} \mathbf{A}^{T} \mathbf{V}_{i}}{\mathbf{A}^{T} \mathbf{1}}$$

which is independent of the material density parameters,  $\gamma_i$ , used in the optimization statement (1).

#### 4.1. Corbel design

This example aims to illustrate the benefits of using a stress-constrained multi-material topology optimization formulation compared to using a single-material formulation. To demonstrate this, we optimize a corbel under three different scenarios: (i) considering a single von Mises candidate material (material 1), (ii) considering a single Drucker–Prager candidate material (material 2), and (iii) considering both materials together as candidate materials. The geometry and boundary conditions for all three design cases are shown in Fig. 4. The corbel is subjected to a load  $P=600\,\mathrm{kN}$ , applied at its tip and distributed over a height d=0.2L. To exploit symmetry, one-half of the domain is discretized into 314,432 eight-node regular hexahedral elements, with symmetry boundary conditions imposed along the x-y plane.

The material properties for each candidate material are summarized in Table 4. As shown in the table, both materials are assumed to be linear elastic, each with a Young's modulus, E = 30 GPa, and a Poisson's ratio, v = 0.2. However, they differ in their yield criteria. Material 1 follows the von Mises yield criterion and has a yield stress of  $\sigma_{lim}$  = 20 MPa, while material 2 is governed by the Drucker-Prager yield criterion, and it is characterized by a uniaxial tensile yield stress of  $\sigma_t$  = 10 MPa and a uniaxial compressive yield stress of  $\sigma_c = 35$  MPa. Note that  $\sigma_t < \sigma_{\rm lim}$  and  $\sigma_c > \sigma_{\rm lim}$  , indicating that the Drucker–Prager material is weaker in tension and stronger in compression compared to the von Mises material. Consequently, in design scenario (iii), the optimizer is expected to assign the von Mises material to tension-dominated regions and the Drucker-Prager material to compression-dominated regions of the domain. This material distribution enables more efficient use of the available materials, resulting in a lighter structure compared to design scenarios (i) and (ii), where only a single candidate material is available.

<sup>&</sup>lt;sup>b</sup> Parameter  $\bar{\beta}$  starts at 1 and increases by  $\bar{\beta}_{\rm inc}$  every  $\bar{\beta}_{\rm freq}$  AL steps and up to a maximum of  $\bar{\beta}_{\rm max}$ .

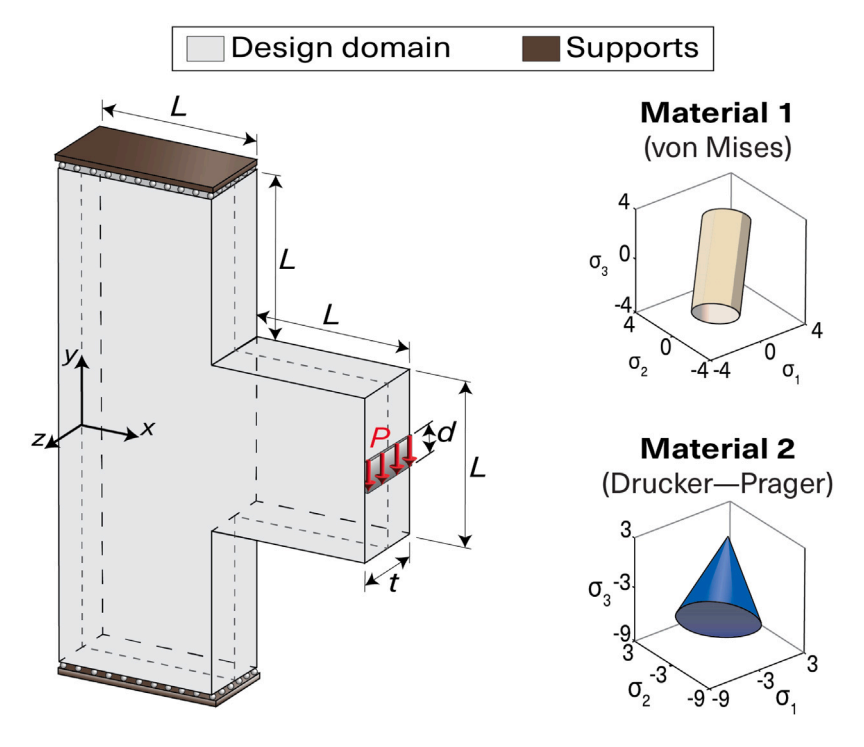


Fig. 4. Geometry, boundary conditions, and candidate materials for the corbel problem. The problem is defined using L=1 m, t=0.5 m, and P=600 kN uniformly distributed across d=0.2 m. The optimizer is allowed to choose between two candidate materials: a von Mises material shown in white and a Drucker-Prager material shown in blue.

**Table 4**Material properties for the multi-material corbel.

FF		
Material property	Material 1	Material 2
Weight factor, $\gamma_i$	1	1
Young's modulus, E (GPa)	30	30
Poisson's ratio, v	0.2	0.2
von Mises stress limit, $\sigma_{lim}$ (MPa)	20	_
Drucker–Prager stress limit in tension, $\sigma_t$ (MPa)	-	10
Drucker–Prager stress limit in compression, $\sigma_c$ (MPa)	-	35

Fig. 5 depicts the results obtained using a filter radius of R = 0.125m. The left column displays the optimized topologies for the three design cases, and the middle column showcases the 3D-printed models. The structures were fabricated using a Bambu Lab A1 multi-color printer and PLA material, solely to demonstrate the manufacturability of the optimized multi-material topologies. Finally, the right column illustrates the normalized equivalent stress maps,  $\tilde{\sigma}^{eq}_{\ell i} = E_{\ell i} \sigma^{eq}_{\ell i}$ , for each of the resulting designs. In design case 1 (Fig. 5a), where only material 1 is used, the optimized topology is symmetric about the horizontal center plane. This symmetry follows from the von Mises criterion, which assumes identical tensile and compressive strengths, thus leading to identical material distributions in tension-dominated and compression-dominated regions of the domain. In design case 2 (Fig. 5b), where only material 2 is considered, the topology becomes asymmetric due to the tension-compression strength asymmetry in the Drucker-Prager criterion. The members in the tension-dominated region are thicker, consistent with the material compressive strength being 3.5 times larger than its tensile strength (see Table 4).

The combined-material case (Fig. 5c) integrates features from both single-material solutions. The tension-dominated region resembles the von Mises case, while the compression-dominated region resembles the Drucker–Prager case. This multi-material topology leverages the strength characteristics of each material: the von Mises material is assigned to regions governed by tensile stresses, whereas the Drucker–Prager material is assigned to compression-dominated zones. The outcome is a 14% reduction in total volume fraction compared with the

single-material designs, as indicated by the optimized values (VF) in Fig. 5. These results demonstrate the capability of the multi-material formulation to achieve lightweight, high-performance structures.

The stress maps and yield surfaces shown on the right column of Fig. 5 confirm that all three designs satisfy the local stress constraints. The equivalent stress values remain less than or equal to one across all elements, indicating that no constraint violations occur. Additionally, the principal stress points evaluated at the centroid of each element lie on or within their respective yield surfaces, further validating constraint satisfaction.<sup>4</sup> In the multi-material design, the equivalent stress distribution exhibits similar patterns to the von Mises stress distribution in the single-material case. In particular, both cases show a pronounced stress concentration at the central joint, the intersection where the members made of von Mises material meet, indicating that the location of maximum stress is preserved between the two designs. This behavior highlights the physical consistency maintained in our approach: each material responds according to its own failure mechanism, and the optimizer naturally assigns each material where it can best meet the local performance demands. This demonstrates the robustness of our

<sup>&</sup>lt;sup>4</sup> Principal stresses are sorted at each evaluation point, i.e.,  $\sigma_1 \geq \sigma_2 \geq \sigma_3$ . The apparent clustering of points toward the  $\sigma_1$  axis results from the principal-stress ordering convention and constitutes a visualization artifact, not a physical bias in the stress distribution.

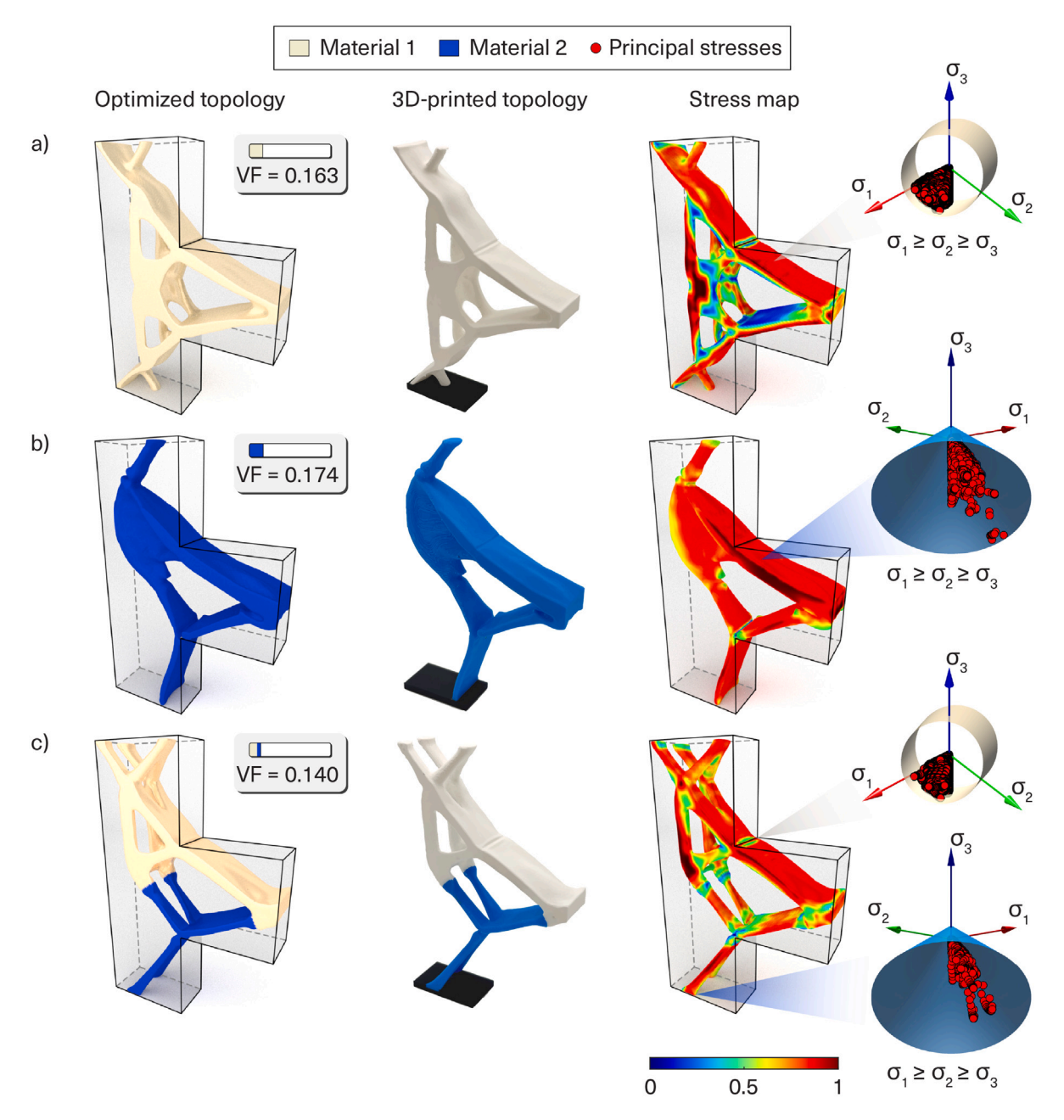


Fig. 5. Optimized topologies (left), and equivalent stress maps (right) for the multi-material corbel design using: (a) a von Mises material, (b) a Drucker–Prager material, and (c) a combination of the two materials. The corresponding yield surfaces (shown in white and blue) and principal stresses (shown in red) for each design case are displayed alongside the stress maps. The 3D-printed corbels (middle), which are 150 mm tall, demonstrate the practical realization of the optimized designs.

formulation in simultaneously respecting distinct yield criteria while effectively handling a large number of stress constraints.

The convergence plots for the three design cases are presented in Fig. C.1 in Appendix C. These plots show the evolution of the maximum equivalent stress and the volume fraction for the three design cases as a function of the AL iterations.

#### 4.2. Airless tire design

This example demonstrates the solution of a multi-material problem involving multiple load cases and pattern repetition, as depicted in Fig. 6. The objective is to design a multi-material airless tire with a radius of  $R_1=40~\mathrm{mm}$  and a thickness of  $t_3=8~\mathrm{mm}$ . Due to symmetry, we only

modeled one-half of the domain and discretized it into 77,200 eight-node regular hexahedral elements, and applied symmetry boundary conditions along the x-y plane. We enforce pattern repetition through a modified filter operator,  $\mathbf{P}$ , which constraints the design space to density fields exhibiting angular symmetry (see [42]). Specifically, as shown in Fig. 6b, we impose periodicity on material distribution every  $\pi/2$  radians, which corresponds to a pattern repetition with  $N_p=4$  [42].

The wheel is subjected to normal and shear tractions representing ground contact forces. To capture variations in the load position as the wheel rotates, three distinct load cases are considered, corresponding to normal and tangential load combinations applied at angular positions  $\alpha=0^\circ$ , 45°, and 90°. For each load case, a distributed normal force of total magnitude F=700~N is applied over an angular span of

 Table 5

 Material properties for the multi-material airless tire.

Material property	Material 1	Material 2	Material 3
Weight factor, $\gamma_i$	0.77	1	10
Young's modulus, E (GPa)	200	200	200
Poisson's ratio, v	0.3	0.3	0.3
Drucker–Prager tension stress limit, $\sigma_t$ (MPa)	120	36	30
Drucker–Prager compression stress limit, $\sigma_c$ (MPa)	36	120	30

 $\theta_0=15^\circ$ , following a cosine distribution. The peak of each distributed load occurs at the angular position,  $\alpha$ , as seen in Fig. 6c. To account for frictional effects, a tangential force is also applied using a friction coefficient  $\mu=1$ , resulting in distributed tangential loads following the same cosine distribution as the normal loads.

For this design, we considered three candidate materials, each modeled using the Drucker–Prager yield criterion to capture the asymmetry between tensile and compressive strengths. This approach enables the optimizer to assign materials based on whether a region is tension- or compression-dominated—something not possible with the von Mises criterion, where only the material with the highest yield strength would be favored. The mechanical properties for these candidate materials are listed in Table 5.

To ensure practical manufacturability, we defined two passive regions. The first, assigned to material 3, forms a uniform layer of thickness  $t_1=2$  mm and located along the outer boundary to provide a smooth and functional contact surface (see Fig. 6). The second, assigned to material 1, is another uniform layer of thickness  $t_2=2$  mm and located along the inner boundary surrounding the fixed nodes. Additionally, a high weight factor,  $\gamma_3=10$ , is used to penalize the use of material 3 elsewhere, ensuring it remains confined to the first passive region.

As discussed before, the multiple load case formulation is detailed in Appendix A. For the airless tire design problem, we consider three load cases and three candidate materials, which results in a total number of stress constraints of  $N_c=9N$ , where N is the number of elements in the mesh. With N=77,200, this results in  $N_c=694,800$  stress constraints that must be handled by the optimizer.

Fig. 7 illustrates the optimized topology and corresponding equivalent stress distributions obtained using a filter radius of R=2.5 mm. Specifically, Figs. 7a-b illustrate the optimized material distribution and the 3D-printed model, respectively,<sup>5</sup> whereas Fig. 7c shows the envelope of the maximum normalized equivalent stress across all load cases.<sup>6</sup> These results show that all candidate materials remain within their respective yield limits. Note that the passive regions in Fig. 7c are presented with the color of their corresponding material as the stress constraints are not evaluated in these regions. Combined, these results highlight the effectiveness of our framework in handling multiple load cases within a multi-material design context. Interested readers are referred to Fig. C.2 in Appendix C, which illustrates the evolution of the volume fraction and the maximum normalized equivalent stress for this problem.

Table 6 summarizes the computational cost for all numerical problems discussed above. All optimization iterations were performed in Matlab R2024b on a desktop computer equipped with an Intel Xeon W-2225 (4.10 GHz) CPU, 64 GB of RAM, and an NVIDIA RTX A4000 GPU. For each problem, the table reports the mesh size, total constraint evaluations, number of MMA iterations, average time per iteration, and total runtime.

From these results, we can observe that treating the stress constraints independently for each material and each element does not inherently result in a significant increase in optimization time. For example, the multi-material corbel problem, despite having roughly four times the number of elements as the airless tire problem, required only about 15% longer to complete. This suggests that the computational framework scales adequately with mesh refinement. However, because the stress and variable-change tolerances differed between the two problems, the total runtime appears to be influenced more by optimization parameters than by the number of elements or stress constraints alone.

#### 5. Experimental validation

In this section, we discuss the experimental validation of our stress-constrained multi-material topology optimization formulation. The validation process began by fabricating test specimens used to measure the elastic modulus and yield strength of two candidate materials under uniaxial tension and uniaxial compression, respectively. The experimentally measured elastic properties and yield strengths were used as inputs for our topology optimization framework, which we used to obtain various optimized beam designs. Finally, we 3D-printed the optimized designs and evaluated their performance via three-point bending tests. This integrated process enables us to assess the predictive capabilities and practical applicability of our framework.

## 5.1. Multi-material 3D printing

In this work, we used PolyJet 3D printing to fabricate both material test specimens used for material characterization and the optimized multi-material beams used for validation of our optimization framework. This 3D printing technology was selected for its ability to fabricate multi-material structures, rather than just multi-color structures, which is essential for validating our optimization framework. Additionally, we selected this 3D printing technology because it offers superior resolution and surface quality [67], which we deemed essential for the experimental validation. In this work, we employed the Stratasys J5 MediJet 3D printer using VeroCyan and Digital ABS, which offer distinct mechanical properties suited for tension- and compression-dominated regions, respectively, as discussed later.

The PolyJet 3D printing process involves a layer-by-layer deposition wherein various photopolymer materials, sprayed using inkjet printing heads, are immediately cured with UV light to solidify and bond each layer [68]. Due to the droplet-level mixing, PolyJet can produce smooth, gradient-like material interfaces, reducing interfacial stress concentrations and promoting a strong bond between materials [64,65]. All test specimens and optimized beams were printed with a glossy finish and oriented on the print bed as shown in Fig. 8. After printing, all specimens were submerged in water for 24 h to dissolve the water-soluble support material (WSS150), polished with Grade No. 00 sandpaper to remove surface imperfections, and conditioned in a light-blocking chamber with air circulation for 48 h to remove residual moisture and ensure consistent material properties before testing.

#### 5.2. Material characterization

To quantify the mechanical properties of the candidate materials (i.e., VeroCyan and Digital ABS), we conducted standardized uniaxial

 $<sup>^5</sup>$  The airless tire design was scaled by a factor of 2.5 to ensure manufacturability, as certain features of the original design were too small to be printed accurately with the nozzle size of the Bambu Lab A1 multi-color printer.

<sup>&</sup>lt;sup>6</sup> The stress maps are symmetrized to reflect the periodicity of the problem, with stresses from the first quadrant mirrored across the domain.

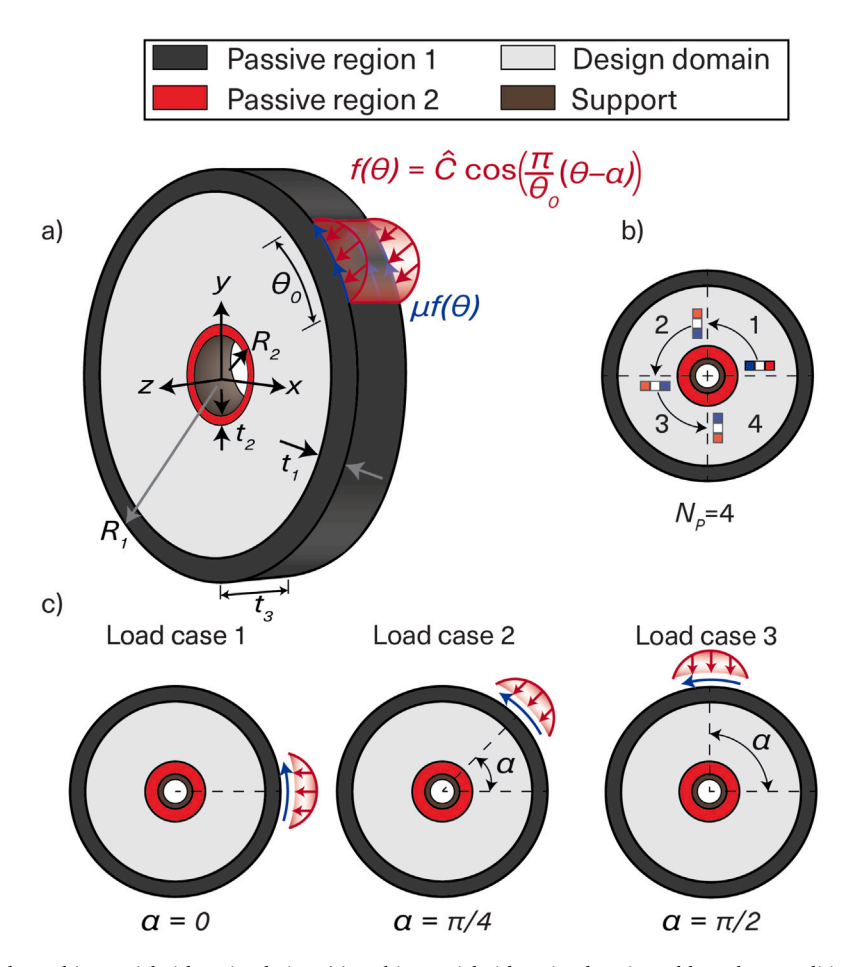


Fig. 6. Problem definition for the multi-material airless tire design. (a) Multi-material airless tire domain and boundary conditions; (b) schematic illustrating the pattern repetition of densities in the design; and (c) the loading cases considered in the design, where the multi-material airless tire is subjected to normal and shear tractions representing the contact forces exerted by the ground on a wheel while neglecting the dynamic effects. The domain is defined using  $R_1 = 40$  mm,  $R_2 = 6$  mm,  $t_1 = 2$  mm,  $t_2 = 2$  mm, and  $t_3 = 8$  mm. The normal traction is given by  $f(\theta) = \hat{C} \cos\left(\frac{\pi}{t_0}(\theta - \alpha)\right)$ , where  $\hat{C}$  is a constant determined such that the total magnitude of the normal force equals F = 700 N,  $\theta_0 = 15^\circ$ , and  $\alpha \in \{0, \pi/4, \pi/2\}$ . The shear traction is given by  $T = \mu f(\theta)$ , where  $\mu = 1.0$ .

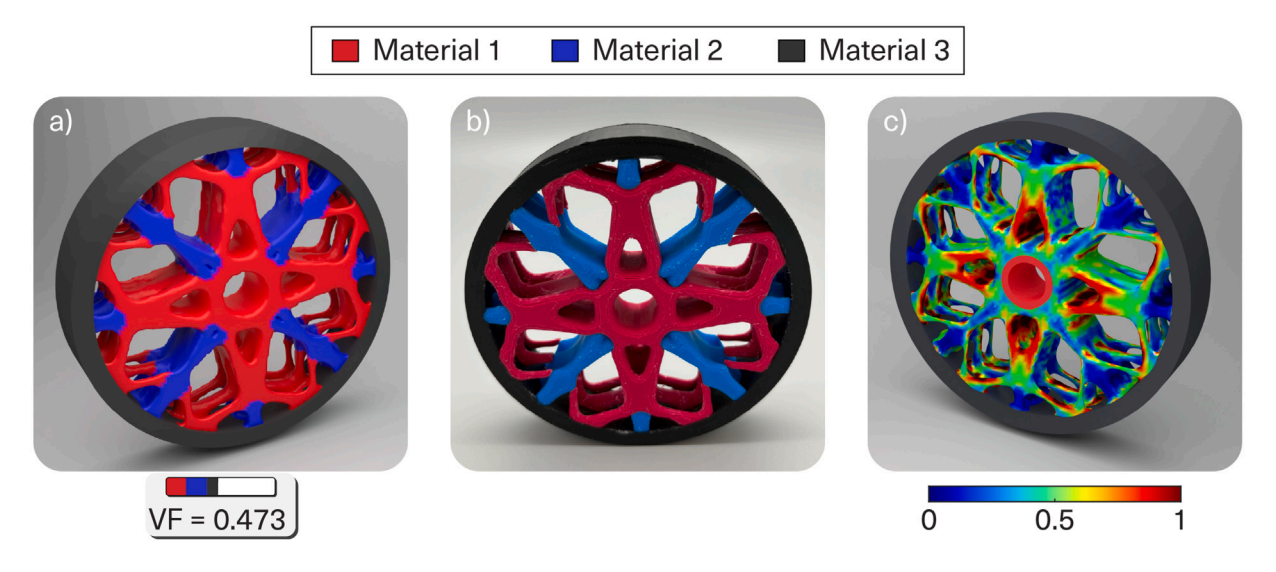


Fig. 7. Multi-material airless tire design with three different candidate materials. (a) Optimized multi-material distribution, (b) 3D-printed airless tire, and (c) equivalent stress map. The resulting design has a volume fraction of 0.473 and was obtained considering the Drucker–Prager yield criterion for the three candidate materials.

tension and compression tests in accordance with ASTM D695 and ASTM D638, respectively [69,70]. For the tensile tests, we adopted

Type IV dogbone specimens, and for the compression tests, we used standard rectangular prisms (see Fig. 8). Each material was tested

Table 6
Computational cost for the numerical benchmark problems in Section 4.

Design problem	Mesh size	Number of constraints	Iterations	Time/iter. (s)	Total time (h)
von Mises corbel	314,432	314,432	224	27.3	1.7
Drucker-Prager corbel	314,432	314,432	393	33.0	3.6
Multi-material corbel	314,432	628,864	182	41.5	2.1
Airless tire	77,200	694,800	236	27.7	1.8

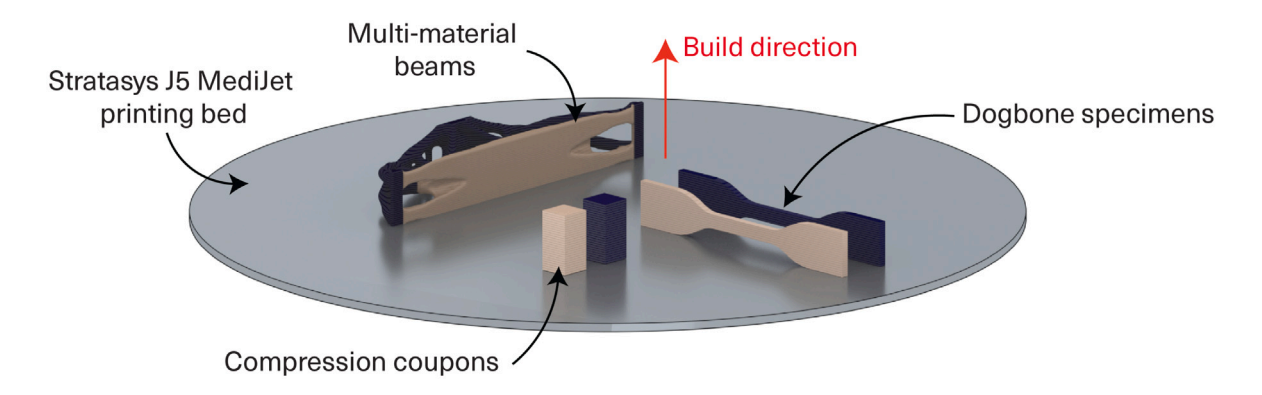


Fig. 8. Printing layout on the Stratasys J5 MediJet printing bed, illustrating the orientation of the specimens used for material characterization, along with a multi-material beam designed based on the measured mechanical properties of the constituent materials.

**Table 7**Material properties for the multi-material beam problem.

Material property	VeroCyan	Digital ABS
Weight factor, $\gamma_i$	1.15	1
Young's modulus, E (MPa)	2,588	2,162
Poisson's ratio, v	0.3	0.3
Uniaxial tension stress limit, $\sigma_t$ (MPa)	37.3	39.6
Uniaxial compression stress limit, $\sigma_c$ (MPa)	74.1	52.9
Equibiaxial compression stress limit, $\sigma_b$ (MPa)	74.1 <sup>a</sup>	52.9 <sup>a</sup>

<sup>&</sup>lt;sup>a</sup> The equibiaxial compression stress limit used in the Willam-Warnke failure criterion was assumed to be equal to the uniaxial compression stress limit due to the lack of experimental testing equipment for biaxial compression tests.

using four specimens per loading mode, with tensile tests conducted at 5 mm/min and compression tests at 1 mm/min using an MTS 370 load frame under displacement-controlled conditions.

Fig. 9 depicts the resulting stress–strain curves for both materials and Table 7 summarizes the corresponding Young's modulus and yield stresses obtained from these curves and employed later in the numerical models. These results show that the Digital ABS has a higher yield stress in tension, whereas the VeroCyan exhibits a greater yield stress in compression. Based on these findings, we anticipate that the optimizer will place Digital ABS in the tension-dominated regions of the beam and VeroCyan in the compression-dominated regions to maximize structural performance while minimizing material usage.

## 5.3. Multi-material beam designs

Using the measured material properties (i.e., the Young's moduli and yield stresses discussed in the previous section), we optimized the topology of a simply supported beam. The beam geometry, loading conditions, supports, and passive regions are illustrated in Fig. 10. The simply supported beam has length L=150 mm, height L/4, and width L/6. For this problem we considered two load cases. The first consists of a vertical load, P=3,000 N, applied over a region of width d=6 mm, and the second consists of a lateral load,  $\alpha P$ , with  $\alpha=0.15$ , distributed over a region of width d=6 mm and height h=6 mm. The lateral load was introduced to mitigate the risk of lateral buckling instabilities observed in preliminary experimental tests conducted on beams designed solely for the vertical load case. Besides considering two load cases, we also considered passive regions of width b=6 mm and thickness t=1.5 mm at the support locations (see Fig. 10) to prevent material removal in these critical areas and to avoid issues related to stress singularities.

To obtain the numerical results discussed next, we discretized half of the beam domain into 98,784 regular hexahedral elements and imposed symmetry boundary conditions along the y-z plane at the midspan location. Additionally, we used a filter radius, R = 6 mm, a convergence tolerance for the design variables, To1 = 0.0015, and a convergence tolerance on the stress constraints, To1S = 0.008. Finally, we employed a continuation scheme on the DMO mixing penalty factor,  $\tau$ , starting

 $<sup>^7</sup>$  The yield stresses in both tension and compression were determined using the 0.2% offset method. According to this method, the yield stress is obtained from the intersection between the stress–strain curve and a line parallel to its elastic region but offset by 0.2% strain on the strain axis. We employed this method because our materials do not exhibit a distinct yield point.

<sup>&</sup>lt;sup>8</sup> We note that buckling constraints are not included in the present formulation, and incorporating them explicitly is part of our future work.

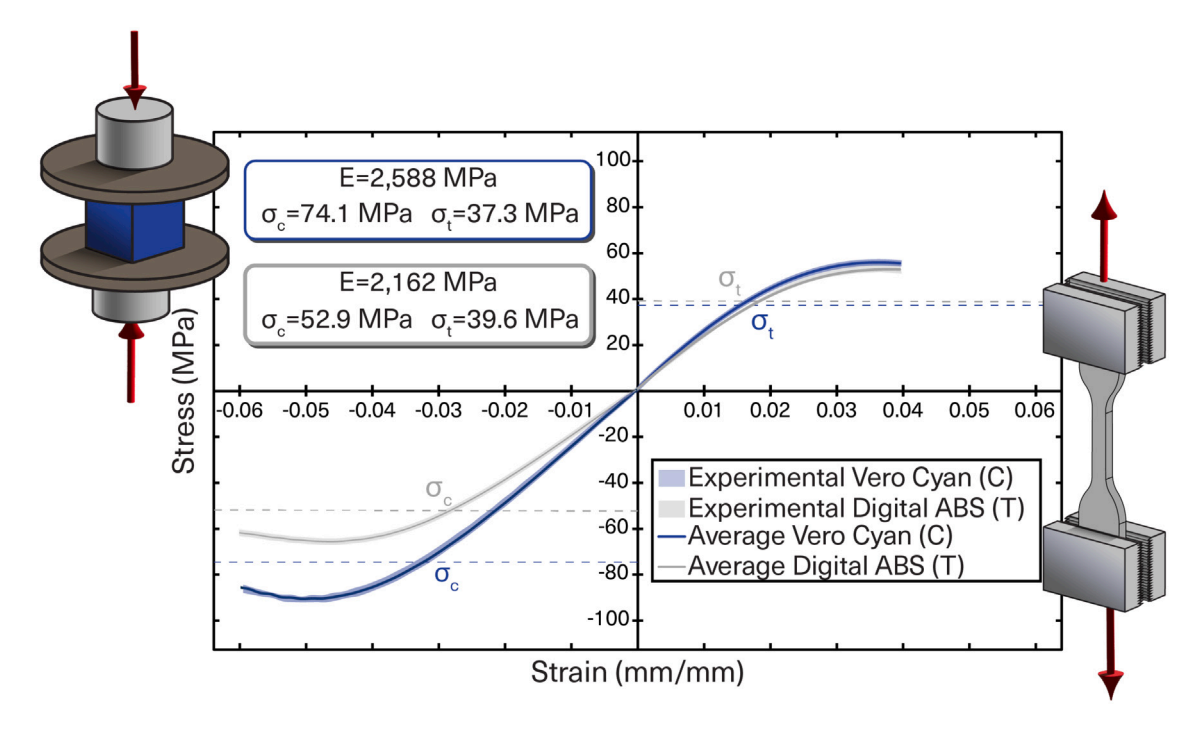
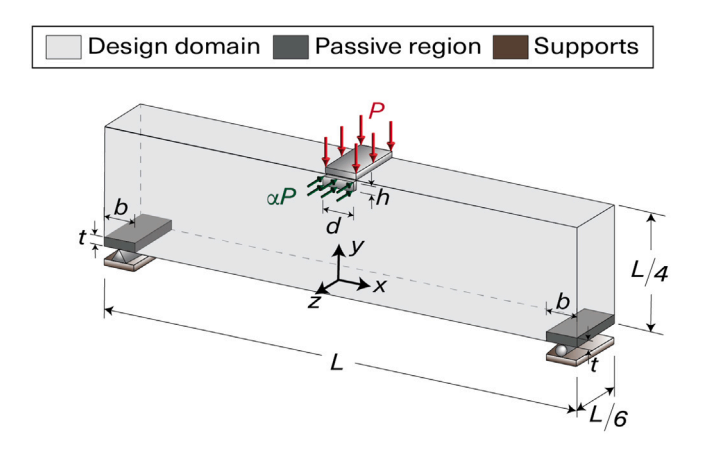


Fig. 9. Stress-strain curves in tension and compression for the two candidate materials: VeroCyan (blue) and Digital ABS (gray).



**Fig. 10.** Geometry and loading conditions for the beam problem. The geometry is defined using L=150 mm, b=6 mm, d=6 mm, h=1.5 mm, t=1.5 mm, load P=3,000 N, and a lateral load applied as a fraction of the vertical load where  $\alpha=0.15$ .

at  $\tau=0$  and increasing incrementally by 0.5 every two AL iterations, until reaching a value of  $\tau=1$ .

To incorporate the tension-compression strength asymmetry into our multi-material formulation, we must select an appropriate yield criterion to characterize the failure behavior of each of the two candidate materials. Given the limited availability of experimental data to know the exact shape of the yield surfaces for our materials, we considered three different yield criteria, namely Drucker–Prager, Mohr–Coulomb, and Willam–Warnke.

Fig. 11 presents the results obtained for each of the yield criteria considered in this study. The left column of Fig. 11 displays the resulting multi-material topologies for each of the three designs. As shown, each yield criterion produced a truss-like structure and, as expected, the optimizer assigned VeroCyan to the compression-dominated regions of the beams and Digital ABS to the tension-dominated regions. The middle column of Fig. 11 shows the resulting 3D-printed topologies. These prints reflect the final geometries obtained after postprocessing, <sup>10</sup> and demonstrate the feasibility of manufacturing complex multi-material structures with sharp material transitions. Finally, the right column of Fig. 11 displays the envelope of equivalent stress maps for each design, showing that all stress constraints were satisfied locally. Because half of the domain was discretized using 98,784 regular hexahedral elements, and we considered two candidate materials and two load cases, our AL-based formulation effectively enforced 395,136 stress constraints.

Fig. 11 illustrates how the choice of the yield criterion influences the optimized volume fraction and the material distribution of the multimaterial designs. The Drucker–Prager criterion produced a total volume fraction of 0.192, while the Willam–Warnke design resulted in the lowest volume fraction of 0.186, and the Mohr–Coulomb design yielded the highest total volume fraction of 0.210. Despite these differences, a consistent trend emerges. Specifically, across all three cases, VeroCyan consistently comprised approximately 56% of the total solid material, with the remainder assigned to Digital ABS. This preference reflects the tendency of the optimizer to exploit the superior compressive capacity of VeroCyan, whose uniaxial compressive yield strength is about 40% higher than that of Digital ABS, while its uniaxial tensile strength is only 6% lower than that of Digital ABS. Consequently, across all three criteria the designs show a modest but consistent bias toward VeroCyan. The evolution of material fractions and maximum equivalent

<sup>&</sup>lt;sup>9</sup> All of these criteria account for different yield stresses in tension and compression but differ in the shape of their yield surfaces and the parameters required to define them. For instance, the Drucker–Prager and Mohr–Coulomb criteria require only uniaxial tensile and compressive yield stresses, whereas the Willam–Warnke criterion requires the yield stress in equibiaxial compression in addition to the two aforementioned yield stresses. Due to the lack of

additional experimental data, we conservatively assume that the yield stress in equibiaxial compression is equal to the yield stress in uniaxial compression.

We postprocessed the resulting material density fields to remove necking artifacts that might compromise the structural performance of the multi-material beams, as detailed in Appendix B.

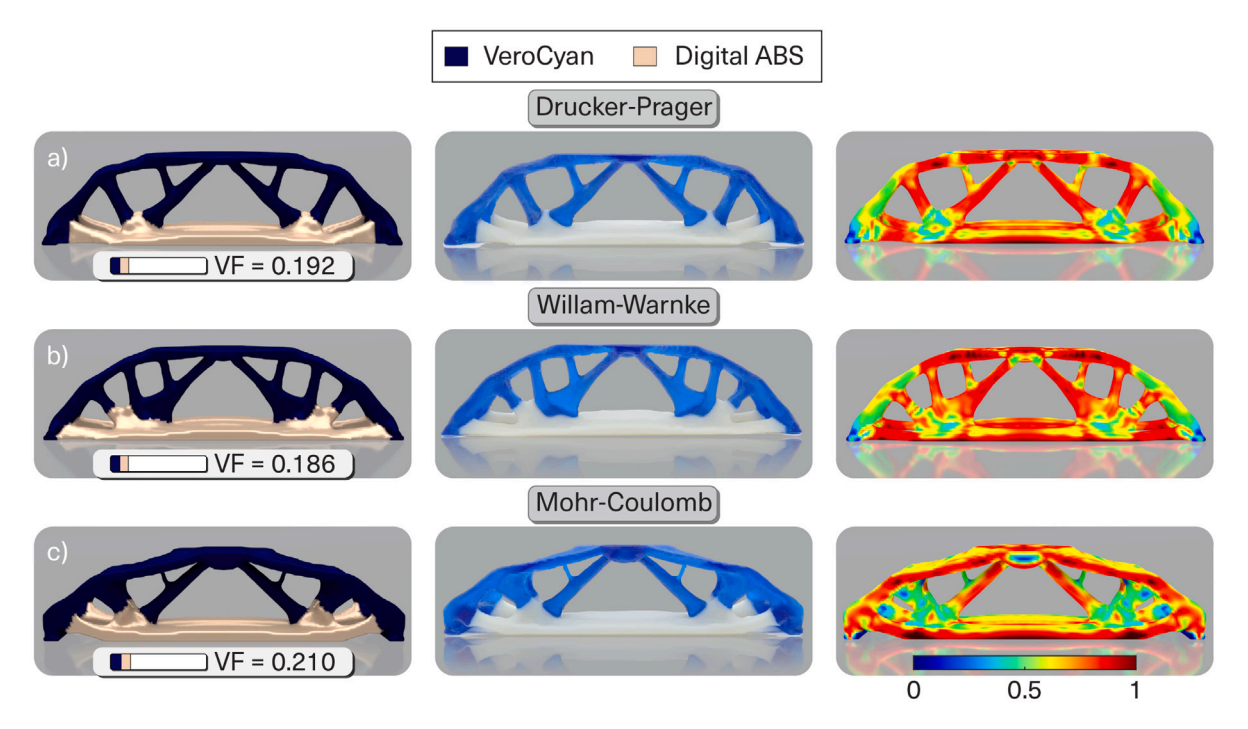


Fig. 11. Multi-material beam designs for different yield criteria: (a) Drucker-Prager, (b) Willam-Warnke, and (c) Mohr-Coulomb. For each criterion, the figure shows the optimized topology (left), the corresponding 3D-printed beam (middle), and the normalized equivalent stress map (right).

stress during the optimization iterations is provided in Fig. C.3 from Appendix C, corroborating these trends.

#### 5.4. Experimental testing and discussion

We evaluated the mechanical performance of the optimized multimaterial beams using three-point bending tests. The setup, illustrated in Fig. 12a, is summarized below:

- 1. We prepared two printed replicas of each optimized beam design shown in Fig. 11 for testing.
- 2. We employed a custom three-point bending fixture to replicate the supports and loading conditions of the numerical model.
- 3. We filed the indenter tip down to a width of 6 mm, corresponding to the dimension *d* in Fig. 10.
- 4. We applied a controlled displacement at the mid-span at a constant rate of 1 mm/min.
- 5. We continuously recorded the reaction force until failure.
- 6. We used a high-speed camera to capture snapshots of each test at the instant of failure.

Fig. 12b shows the load-displacement curves obtained from the three-point bending tests. The beam designed using the Drucker-Prager yield criterion failed at a maximum load of 2051 N, which is 32% lower than the design load of 3000 N. The beam designed with the Willam-Warnke criterion reached a peak load of 2728 N, falling short of the design load by 9%. Similarly, the Mohr-Coulomb design failed at 2636 N, underestimating the design load by 12%. All beams failed with displacements below 6 mm. This behavior is consistent with our earlier findings that stress-constrained solutions yield compliance values of the same order of magnitude as minimum-compliance formulations [42], since stress constraints indirectly limit the overall deflection of the optimized structure. Interestingly, despite the constituent materials exhibiting ductile behavior in uniaxial tests (see Fig. 9), the Drucker-Prager and Willam-Warnke beams exhibited brittle failure, whereas the Mohr-Coulomb design showed signs of minor plastic deformation prior to failure, suggesting a slightly more ductile response compared to the other two designs.

Fig. 12c shows high-speed camera snapshots captured at the instant of failure for each beam design. In all cases, failure initiated at one of the top joints, rather than in the regions predicted to exhibit the highest equivalent stresses (see the right column of Fig. 11). This discrepancy in failure location, coupled with the premature failure observed during testing, may be attributed to several contributing factors.

First, the stress state at the failure locations differs significantly from the uniaxial stress conditions used during material characterization. As a result, the selected yield criteria may be inadequate for predicting failure of the candidate materials under complex multiaxial stress states. Additional testing, including biaxial tension and compression tests, could provide more information to identify the most accurate shape of the yield surfaces needed to model the failure behavior of the candidate materials. Second, all yield criteria used in this study assume isotropic material behavior and do not account for the anisotropy induced by the PolyJet printing process. Prior work has shown that the mechanical properties of PolyJet-printed components are sensitive to print orientation [71-73]. As shown in Fig. 8, the tensile specimens were printed with the layer lines aligned with the loading direction, while the compression specimens had layers oriented perpendicular to the load. These print orientations represent idealized conditions leading to the highest possible uniaxial yield strengths, which can result in the overestimation of the actual strength in more complex, multiaxial stress states experienced by the optimized beams. Finally, potential manufacturing defects, such as internal voids, may also have contributed to the observed failure modes by locally reducing material strength [74].

Despite the fact that the beams did not reach their intended design load, the experimental results demonstrate that our model captures the structural capacity of the multi-material beams with reasonable accuracy. It should be emphasized that this validation is limited to components fabricated at the tested laboratory scale using PolyJetprinted photopolymers, and the results may not directly extend to larger-scale structural applications or to parts manufactured by other additive manufacturing technologies. Possible extensions could incorporate anisotropic yield criteria such as the Tsai–Wu [75] and the Liu-Huang-Stout [76] criteria, which may enable the framework to

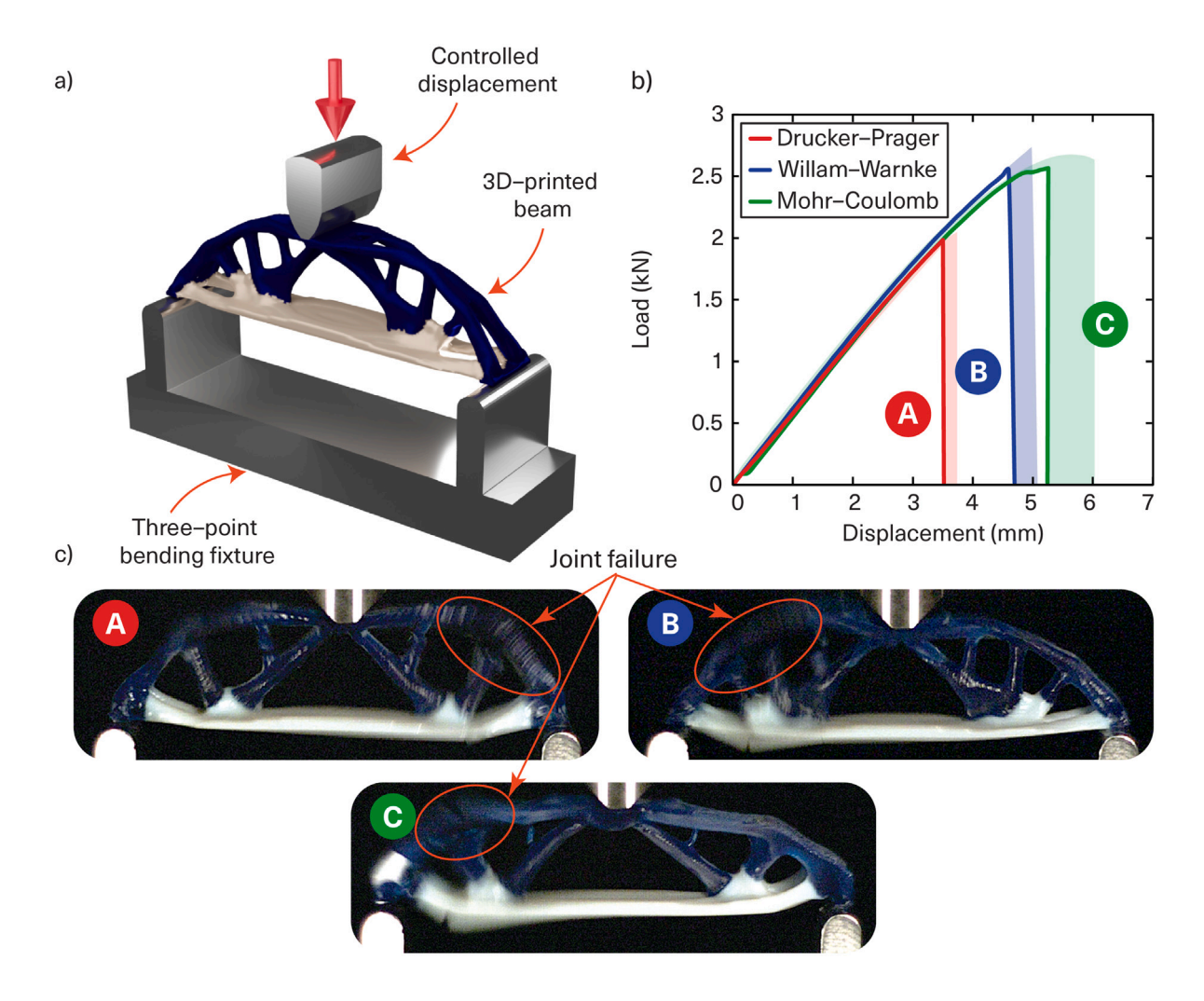


Fig. 12. Experimental validation of the multi-material beam topologies. (a) Test setup, (b) load–displacement curves comparing the performance under different yield criteria, and (c) high-speed snapshots capturing the failure mechanisms at maximum load for specimens corresponding to each yield criterion.

**Table 8**Computational cost for the experimental validation problems in Section 5.

	1				
Design problem	Mesh size	Number of constraints	Iterations	Time/iter. (s)	Total time (h)
Drucker–Prager beam	98,784	395,136	228	27.3	1.7
Willam-Warnke beam	98,784	395,136	273	26.4	2.0
Mohr-Coulomb beam	98,784	395,136	254	29.7	2.1

more accurately model material behavior across different manufacturing processes and length scales, including structural-scale components.

For completeness, Table 8 summarizes the computational cost for the experimental validation problems presented in this section. The reported runtimes were obtained using the same computing environment described in Section 4. As in the numerical benchmarks, the table lists the mesh size, total constraint evaluations, number of MMA iterations, average time per iteration, and total runtime.

## 5.5. Limitations and future work

While this work advances the field of stress-constrained multimaterial topology optimization, our validation was limited to Poly-Jet printing, which produces smooth, gradient-like interfaces through droplet-level material mixing. This process minimizes interfacial stresses and promotes strong bonding between materials [64,65], justifying the omission of interfacial stress constraints in our work. However, weaker interfaces are often encountered in other additive manufacturing processes, such as fused deposition modeling (FDM), where imperfect interlayer adhesion frequently governs failure. In such cases, explicitly modeling interfacial failure becomes essential to ensure reliable model predictions. Another important direction is the incorporation of material mixing models, which would allow the framework to represent graded transitions between materials. Such gradients, inspired by biological systems, can reduce stress concentrations and improve load transfer across interfaces, but they require constitutive descriptions of intermediate mixtures that go beyond the discrete material phases considered here. Extending the framework with both interface-specific stress constraints and material mixing models could

therefore broaden its applicability and capture a wider range of bonding behaviors across additive manufacturing processes and material systems.

Beyond interfacial considerations, the mechanical response of Poly-Jet parts is also known to depend strongly on build orientation. Prior studies have reported orientation-dependent anisotropy in PolyJetprinted parts [71-73], and additional modeling uncertainty may arise from unquantified manufacturing defects such as internal voids. Although a rigorous experimental characterization of yield behavior, including biaxial tension-compression testing of base materials and systematic quantification of print-orientation effects, is outside the scope of the present study, such efforts would substantially improve the predictive capabilities of the computational framework and help close the gap between numerical predictions and the performance of physical prototypes. We are currently working in this direction by extending the formulation to account for anisotropic yield criteria (e.g., Tsai-Wu [75] and Liu-Huang-Stout [76]), which will allow the framework to better capture orientation-dependent effects and broaden its applicability to a wider class of materials and processes. To enable practical application to the design of large-scale structures, future research could also explore additional manufacturing technologies and explicitly incorporate manufacturing uncertainties.

Besides process-related considerations, geometric nonlinearities and structural-scale effects also present important directions for future extension. In the beam example, a lateral load was introduced to mitigate the risk of buckling observed in preliminary tests, but buckling itself was not considered in the formulation. Incorporating such constraints directly will be an important next step to ensure that optimized structures reach their yield limit before experiencing geometric instabilities. Another natural extension of the framework is the inclusion of displacement constraints, which would allow serviceability limits to be enforced explicitly. Such constraints can restrict excessive nodal deflections, thereby ensuring that the small-deformation assumptions adopted in the present study remain valid. By combining stress, stability, and displacement considerations, the formulation could potentially address both strength and serviceability requirements in a unified optimization setting. Overall, these developments will extend the applicability of the framework to more realistic structural-scale problems and reinforce its potential as a robust, high-fidelity tool for the design of multimaterial structures under complex mechanical constraints, with strong applications in additive manufacturing, lightweight design, and the optimization of functional, mechanically resilient systems.

## 6. Concluding remarks

This work introduced a unified framework for stress-constrained topology optimization of multi-material structures, addressing the critical need to incorporate distinct failure criteria for each candidate material. Building upon the unified yield criterion from our previous work [1], the framework introduced in this study enables the design of structures composed of a wide range of materials exhibiting either pressure-dependent or pressure-independent failure behavior. In contrast to existing approaches, which approximate yielding behavior via nonlinear interpolation between multiple yield criteria, our method enforces one stress constraint per element and per candidate material. This direct enforcement eliminates several key drawbacks of interpolation-based schemes: (i) additional nonlinearities introduced by the interpolation functions, (ii) the need for parameter tuning to control the blending behavior, (iii) inaccurate representation of material yielding during early optimization stages when material mixing is common, and (iv) the risk of overestimating material strength that happens with some interpolation functions. In addition to these advantages, our approach remains computationally efficient. Although we impose one constraint per element and candidate material, we solve the resulting highly constrained optimization problem using the AL method, which requires computing only a single adjoint vector per

load case at each optimization step. From the mathematical structure of the optimization problem, the computational cost of our approach is expected to remain comparable to that of methods based on yield function interpolation. This is because the dominant operations, which include solving the displacement problem, evaluating stresses in all elements and candidate materials, and computing one adjoint problem per load case, are identical in both approaches. Consequently, the overall number of floating-point operations should be approximately the same in either approach.

We demonstrated the capabilities of our approach through a series of three-dimensional numerical examples involving different geometries, loading scenarios, and yield criteria. These examples included design problems such as a multi-material corbel and an airless tire, which showed the scalability of our approach. In the corbel example, the optimizer effectively leveraged the distinct strengths of each candidate material, producing a multi-material design with significantly lower volume fraction than single-material designs. This result highlights the potential of the framework to reduce mass without compromising structural integrity by strategically allocating materials based on local stress demands. In the airless tire problem, our framework successfully handled nearly 700,000 local stress constraints resulting from 77,200 finite elements, three candidate materials, and three load cases, with one constraint imposed per element and material for each load case. Despite the high constraint count, the method achieved stable convergence and produced physically interpretable, manufacturable designs. These results confirm that the method not only scales to large-scale, realistic design problems but also generates efficient structures that satisfy stress constraints locally.

In addition to the numerical examples, we performed experimental testing on optimized multi-material beams fabricated via PolyJet 3D printing to assess the capabilities of the proposed approach to design structures that perform as intended. The designs were based on the Drucker-Prager, Willam-Warnke, and Mohr-Coulomb yield criteria and were evaluated under three-point bending. The beam designed with the Drucker-Prager criterion failed at a maximum load 30% below the intended design load, while the Willam-Warnke and Mohr-Coulomb designs failed, respectively, at a maximum load 12% and 9% below the design load. Although all beams failed before reaching their design load, the experimental results indicate that our model captures the structural response of the multi-material designs with reasonable accuracy. The observed discrepancies between the numerical predictions and the experimental results suggest limitations in the use of isotropic yield criteria and highlight the need to account for print-induced anisotropy.

## CRediT authorship contribution statement

**Juan P. Giraldo-Isaza:** Writing – original draft, Validation, Software development, Investigation. **Oliver Giraldo-Londoño:** Writing – review & editing, Validation, Supervision, Software development, Investigation, Conceptualization.

#### Declaration of competing interest

The authors declare that they have no known competing financial interests or personal relationships that could have appeared to influence the work reported in this paper.

#### Acknowledgments

The authors are grateful for the endowment provided by the James W. and Joan M. O'Neill Faculty Scholar in Engineering at the University of Missouri. The findings and conclusions presented in this study are solely those of the authors and do not necessarily reflect the views of the sponsors. All authors have reviewed and approved the final version of the manuscript for publication.

## Appendix A. Sensitivity analysis

Based on our previous work [1,2,42,77], we use the AL method to find the solution of the constrained optimization problem (1) as a sequence of unconstrained optimization sub-problems, each aiming to minimize the AL function. Specifically, at each step k of the AL method we solve the following minimization problem:

$$\min_{\mathbf{z} \in [0,1]^{N \times m}} J^{(k)}(\mathbf{z}, \mathbf{u}) = f(\mathbf{z}) + \frac{1}{mN} P(\mathbf{z}, \mathbf{u}), \ k = 0, 1, 2, ...$$
 (27)

where  $f(\mathbf{z})$  is the objective function and  $P(\mathbf{z}, \mathbf{u})$  is a penalization term, which is given by:

$$P(\mathbf{z}, \mathbf{u}) = \sum_{i=1}^{m} \sum_{\ell=1}^{N} \left[ \lambda_{\ell i}^{(k)} h_{\ell i}(\mathbf{z}, \mathbf{u}) + \frac{\mu^{(k)}}{2} h_{\ell i}^{2}(\mathbf{z}, \mathbf{u}) \right].$$
 (28)

We approximately solve each optimization sub-problem using a gradient-based algorithm. Accordingly, we evaluate the sensitivity of (27) using the chain rule, as follows:

$$\frac{\partial J^{(k)}}{\partial \mathbf{z}} = \frac{\partial \mathbf{E}}{\partial \mathbf{z}} \frac{\partial J^{(k)}}{\partial \mathbf{E}} + \frac{\partial \mathbf{V}}{\partial \mathbf{z}} \frac{\partial J^{(k)}}{\partial \mathbf{V}} + \frac{\partial \mathbf{W}}{\partial \mathbf{z}} \frac{\partial J^{(k)}}{\partial \mathbf{W}}, \tag{29}$$

where 
$$\mathbf{E} = \{E_{\ell 1}, \dots, E_{\ell m}\}_{\ell = 1}^{N}, \quad \mathbf{V} = \{V_{\ell 1}, \dots, V_{\ell m}\}_{\ell = 1}^{N}, \quad \mathbf{M} = \{W_{\ell 1}, \dots, W_{\ell m}\}_{\ell = 1}^{N}, \quad \mathbf{M} = \{W_{\ell 1}, \dots, W_{\ell m}\}_{\ell = 1}^{N}, \quad \mathbf{M} = \{W_{\ell 1}, \dots, W_{\ell m}\}_{\ell = 1}^{N}, \quad \mathbf{M} = \{W_{\ell 1}, \dots, W_{\ell m}\}_{\ell = 1}^{N}, \quad \mathbf{M} = \{W_{\ell 1}, \dots, W_{\ell m}\}_{\ell = 1}^{N}, \quad \mathbf{M} = \{W_{\ell 1}, \dots, W_{\ell m}\}_{\ell = 1}^{N}, \quad \mathbf{M} = \{W_{\ell 1}, \dots, W_{\ell m}\}_{\ell = 1}^{N}, \quad \mathbf{M} = \{W_{\ell 1}, \dots, W_{\ell m}\}_{\ell = 1}^{N}, \quad \mathbf{M} = \{W_{\ell 1}, \dots, W_{\ell m}\}_{\ell = 1}^{N}, \quad \mathbf{M} = \{W_{\ell 1}, \dots, W_{\ell m}\}_{\ell = 1}^{N}, \quad \mathbf{M} = \{W_{\ell 1}, \dots, W_{\ell m}\}_{\ell = 1}^{N}, \quad \mathbf{M} = \{W_{\ell 1}, \dots, W_{\ell m}\}_{\ell = 1}^{N}, \quad \mathbf{M} = \{W_{\ell 1}, \dots, W_{\ell m}\}_{\ell = 1}^{N}, \quad \mathbf{M} = \{W_{\ell 1}, \dots, W_{\ell m}\}_{\ell = 1}^{N}, \quad \mathbf{M} = \{W_{\ell 1}, \dots, W_{\ell m}\}_{\ell = 1}^{N}, \quad \mathbf{M} = \{W_{\ell 1}, \dots, W_{\ell m}\}_{\ell = 1}^{N}, \quad \mathbf{M} = \{W_{\ell 1}, \dots, W_{\ell m}\}_{\ell = 1}^{N}, \quad \mathbf{M} = \{W_{\ell 1}, \dots, W_{\ell m}\}_{\ell = 1}^{N}, \quad \mathbf{M} = \{W_{\ell 1}, \dots, W_{\ell m}\}_{\ell = 1}^{N}, \quad \mathbf{M} = \{W_{\ell 1}, \dots, W_{\ell m}\}_{\ell = 1}^{N}, \quad \mathbf{M} = \{W_{\ell 1}, \dots, W_{\ell m}\}_{\ell = 1}^{N}, \quad \mathbf{M} = \{W_{\ell 1}, \dots, W_{\ell m}\}_{\ell = 1}^{N}, \quad \mathbf{M} = \{W_{\ell 1}, \dots, W_{\ell m}\}_{\ell = 1}^{N}, \quad \mathbf{M} = \{W_{\ell 1}, \dots, W_{\ell m}\}_{\ell = 1}^{N}, \quad \mathbf{M} = \{W_{\ell 1}, \dots, W_{\ell m}\}_{\ell = 1}^{N}, \quad \mathbf{M} = \{W_{\ell 1}, \dots, W_{\ell m}\}_{\ell = 1}^{N}, \quad \mathbf{M} = \{W_{\ell 1}, \dots, W_{\ell m}\}_{\ell = 1}^{N}, \quad \mathbf{M} = \{W_{\ell 1}, \dots, W_{\ell m}\}_{\ell = 1}^{N}, \quad \mathbf{M} = \{W_{\ell 1}, \dots, W_{\ell m}\}_{\ell = 1}^{N}, \quad \mathbf{M} = \{W_{\ell 1}, \dots, W_{\ell m}\}_{\ell = 1}^{N}, \quad \mathbf{M} = \{W_{\ell 1}, \dots, W_{\ell m}\}_{\ell = 1}^{N}, \quad \mathbf{M} = \{W_{\ell 1}, \dots, W_{\ell m}\}_{\ell = 1}^{N}, \quad \mathbf{M} = \{W_{\ell 1}, \dots, W_{\ell m}\}_{\ell = 1}^{N}, \quad \mathbf{M} = \{W_{\ell 1}, \dots, W_{\ell m}\}_{\ell = 1}^{N}, \quad \mathbf{M} = \{W_{\ell 1}, \dots, W_{\ell m}\}_{\ell = 1}^{N}, \quad \mathbf{M} = \{W_{\ell 1}, \dots, W_{\ell m}\}_{\ell = 1}^{N}, \quad \mathbf{M} = \{W_{\ell 1}, \dots, W_{\ell m}\}_{\ell = 1}^{N}, \quad \mathbf{M} = \{W_{\ell 1}, \dots, W_{\ell m}\}_{\ell = 1}^{N}, \quad \mathbf{M} = \{W_{\ell 1}, \dots, W_{\ell m}\}_{\ell = 1}^{N}, \quad \mathbf{M} = \{W_{\ell 1}, \dots, W_{\ell m}\}_{\ell = 1}^{N}, \quad \mathbf{M} = \{W_{\ell 1}, \dots, W_{\ell m}\}_{\ell = 1}^{N}, \quad \mathbf{M} = \{W_{\ell 1}, \dots, W_{\ell m}\}_{\ell = 1}^{N}, \quad \mathbf{M} = \{W_{\ell 1}, \dots, W_{\ell m}\}_{\ell = 1}^{N}, \quad \mathbf{M} = \{W_{\ell 1}, \dots, W_{\ell m}\}_{\ell = 1}^{N}, \quad \mathbf{M} = \{W_{\ell 1$$

Based on the functional form of the AL function in (27), we rewrite

$$\frac{\partial J}{\partial z_{\ell i}} = \frac{\partial f}{\partial \mathbf{E}_{i}} \cdot \frac{\partial \mathbf{E}_{i}}{\partial z_{\ell i}} + \frac{\partial f}{\partial \mathbf{V}_{i}} \cdot \frac{\partial \mathbf{V}_{i}}{\partial z_{\ell i}} + \frac{\partial f}{\partial \mathbf{W}_{i}} \cdot \frac{\partial \mathbf{W}_{i}}{\partial z_{\ell i}} + \frac{1}{mN} \left( \frac{\partial P}{\partial \mathbf{E}_{i}} \cdot \frac{\partial \mathbf{E}_{i}}{\partial z_{\ell i}} + \frac{\partial P}{\partial \mathbf{V}_{i}} \cdot \frac{\partial \mathbf{V}_{i}}{\partial z_{\ell i}} + \frac{\partial P}{\partial \mathbf{W}_{i}} \cdot \frac{\partial \mathbf{W}_{i}}{\partial z_{\ell i}} \right).$$
(30)

To simplify the notation, we have dropped the superscript k in (30) and in the subsequent equations of this section.

Given the structure of the objective function in the optimization problem (1), we obtain the following:

$$\frac{\partial f}{\partial V_{\ell i}} = \frac{\gamma_i A_{\ell}}{\sum_{k=1}^{m} \gamma_k \mathbf{A}^T \mathbf{1}} \quad \text{and} \quad \frac{\partial f}{\partial W_{\ell i}} = 0. \tag{31}$$

Additionally, from (24), and (7) we obtain

$$\frac{\partial P}{\partial V_{\ell i}} = 0, \qquad \frac{\partial P}{\partial W_{\ell i}} = 0,$$
 (32)

$$\frac{\partial P}{\partial E_{\ell i}} = \sum_{k=1}^{m} \sum_{i=1}^{N} \left[ \lambda_{jk} + \mu h_{jk} \left( \mathbf{z}, \mathbf{u} \right) \right] \left[ \frac{\partial h_{jk} \left( \mathbf{z}, \mathbf{u} \right)}{\partial E_{\ell i}} + \frac{\partial h_{jk} \left( \mathbf{z}, \mathbf{u} \right)}{\partial \mathbf{u}} \cdot \frac{\partial \mathbf{u}}{\partial E_{\ell i}} \right]. \quad (33)$$

To avoid the expensive computation of  $\partial \mathbf{u}/\partial E_{\ell i}$ , we use the adjoint method to obtain  $\partial P/\partial E_{\ell i}$ . That is, we add the sensitivity of the equilibrium equation, Ku = F, to (33). By doing so, we obtain

$$\begin{split} \frac{\partial P}{\partial E_{\ell i}} &= \sum_{k=1}^{m} \sum_{j=1}^{N} \left[ \lambda_{jk} + \mu h_{jk} \left( \mathbf{z}, \mathbf{u} \right) \right] \left[ \frac{\partial h_{jk} \left( \mathbf{z}, \mathbf{u} \right)}{\partial E_{\ell i}} + \frac{\partial h_{jk} \left( \mathbf{z}, \mathbf{u} \right)}{\partial \mathbf{u}} \cdot \frac{\partial \mathbf{u}}{\partial E_{\ell i}} \right] \\ &+ \xi^{T} \left( \mathbf{K} \frac{\partial \mathbf{u}}{\partial E_{\ell i}} + \frac{\partial \mathbf{K}}{\partial E_{\ell i}} \mathbf{u} \right). \end{split}$$
We collect all the terms in (34) involving  $\frac{\partial \mathbf{u}}{\partial E_{\ell i}}$  which results in:

$$\begin{split} \frac{\partial P}{\partial E_{\ell i}} &= \sum_{k=1}^{m} \sum_{j=1}^{N} \left[ \lambda_{jk} + \mu h_{jk}(\mathbf{z}, \mathbf{u}) \right] \frac{\partial h_{jk}(\mathbf{z}, \mathbf{u})}{\partial E_{\ell i}} \\ &+ \left( \sum_{k=1}^{m} \sum_{j=1}^{N} \left[ \lambda_{jk} + \mu h_{jk}(\mathbf{z}, \mathbf{u}) \right] \frac{\partial h_{jk}(\mathbf{z}, \mathbf{u})}{\partial \mathbf{u}} + \boldsymbol{\xi}^{T} \mathbf{K} \right) \frac{\partial \mathbf{u}}{\partial E_{\ell i}} + \boldsymbol{\xi}^{T} \frac{\partial \mathbf{K}}{\partial E_{\ell i}} \mathbf{u}, \end{split}$$

$$(35)$$

and select the adjoint vector  $\xi$  such that these terms vanish, leading to the following expression:

$$\frac{\partial P}{\partial E_{\ell i}} = \sum_{k=1}^{m} \sum_{j=1}^{N} \left[ \lambda_{jk} + \mu h_{jk} \left( \mathbf{z}, \mathbf{u} \right) \right] \frac{\partial h_{jk} \left( \mathbf{z}, \mathbf{u} \right)}{\partial E_{\ell i}} + \boldsymbol{\xi}^{T} \frac{\partial \mathbf{K}}{\partial E_{\ell i}} \mathbf{u}, \tag{36}$$

where  $\xi$  solves the adjoint problem:

$$\mathbf{K}\boldsymbol{\xi} = -\sum_{k=1}^{m} \sum_{i=1}^{N} \left[ \lambda_{jk} + \mu h_{jk} \left( \mathbf{z}, \mathbf{u} \right) \right] \frac{\partial h_{jk} \left( \mathbf{z}, \mathbf{u} \right)}{\partial \mathbf{u}}.$$
 (37)

Using Eq. (4), the sensitivity of the stiffness matrix with respect to  $E_{\ell i}$ , which is required to evaluate  $\partial P/\partial E_{\ell i}$  in (36), is computed as

$$\frac{\partial \mathbf{K}}{\partial E_{\ell i}} = \sum_{\ell=1}^{N} \sum_{k=1}^{m} \frac{\partial W_{\ell k}}{\partial E_{\ell i}} \mathbf{k}_{\ell k},\tag{38}$$

$$\frac{\partial W_{\ell k}}{\partial E_{\ell i}} = \begin{cases}
\prod_{\substack{j=1\\j\neq k, j\neq i}}^{m} \left(1 - \tau E_{\ell j}\right) & \text{if } k = i \\
-\tau E_{\ell k} \prod_{\substack{j=1\\j\neq k, j\neq i}}^{m} \left(1 - \tau E_{\ell j}\right) & \text{if } k \neq i
\end{cases}$$
(39)

and  $\mathbf{k}_{\ell k}$  is the element stiffness matrix of element  $\ell$  when filled entirely with material k.

The remaining terms necessary for computing  $\partial P/\partial E_{\ell i}$  are  $\partial h_{jk}/\partial E_{\ell i}$  and  $\partial h_{jk}/\partial \mathbf{u}$ , and these are derived below for completeness. For instance,  $\partial h_{ik}/\partial E_{\ell i}$  is obtained explicitly using Eq. (24) and the definition of  $g_{\ell_i}(\mathbf{z}, \mathbf{u})$  given in Eq. (7), as shown below:

$$\frac{\partial h_{jk}(\mathbf{z}, \mathbf{u})}{\partial E_{\ell i}} = \begin{cases} A_{jk} \left( A_{jk}^2 + 1 \right) \delta_{j\ell} \delta_{ki} & \text{when } \mathbf{g}_{jk}(\mathbf{z}, \mathbf{u}) < -\frac{\lambda_{jk}}{\mu} \\ 0 & \text{otherwise,} \end{cases}$$
(40)

where  $\delta_{i\ell}$  is the Kronecker delta operator. Moreover,  $\partial h_{ik}/\partial \mathbf{u}$  is also obtained from Eq. (24) and using the chain rule as follows:

$$\begin{split} &\frac{\partial h_{jk}\left(\mathbf{z},\mathbf{u}\right)}{\partial \mathbf{u}} \\ &= \begin{cases} \frac{\partial g_{jk}}{\partial A_{jk}} \left(\frac{\partial A_{jk}}{\partial I_1} \frac{\partial I_1}{\partial \sigma_{jk}} + \frac{\partial A_{jk}}{\partial J_2} \frac{\partial J_2}{\partial \sigma_{jk}} + \frac{\partial A_{jk}}{\partial J_3} \frac{\partial J_3}{\partial \sigma_{jk}} \right) \cdot \frac{\partial \sigma_{jk}}{\partial \mathbf{u}} & \text{when } \mathbf{g}_{jk}(\mathbf{z},\mathbf{u}) < -\frac{\lambda_{jk}}{\mu} \\ \mathbf{0} & \text{otherwise.} \end{cases} \end{split} \tag{41}$$

The sensitivities of the stress invariants  $I_1$ ,  $J_2$ , and  $J_3$ , with respect to the vector of Cauchy stresses are given by

$$\frac{\partial I_1}{\partial \sigma_{jk}} = \overline{\mathbf{M}}^T, \qquad \frac{\partial J_2}{\partial \sigma_{jk}} = \frac{2}{3} \overline{\mathbf{V}} \sigma_{jk}, \quad \text{and} 
\frac{\partial J_3}{\partial \sigma_{jk}} = \begin{bmatrix}
s_{22}s_{33} - \sigma_{23}^2 \\ s_{11}s_{33} - \sigma_{13}^2 \\ s_{11}s_{22} - \sigma_{12}^2 \\ 2\left(\sigma_{13}\sigma_{12} - s_{11}\sigma_{23}\right) \\ 2\left(\sigma_{12}\sigma_{23} - s_{22}\sigma_{13}\right) \\ 2\left(\sigma_{12}\sigma_{12} - s_{22}\sigma_{13}\right) \\ 2\left(\sigma_{12}\sigma_{23} - s_{22}\sigma_{13}\right) \\ 2\left(\sigma_{12}\sigma_{12} - s_{22}\sigma_{13}\right) \\ 2\left(\sigma_{12}\sigma_{12} - s_{22}\sigma_{13}\right) \\ 2\left(\sigma_{12}\sigma_{12} - s_{22}\sigma_{13}\right) \\ 2\left(\sigma_{12}\sigma_{12} - s_{22}\sigma_{13}\right)$$

for 3D problems and

$$\frac{\partial J_3}{\partial \sigma_{ik}} = \frac{1}{3} \left( J_2 - \frac{1}{3} I_1^2 \right) \overline{\mathbf{M}}^T + \frac{2}{9} I_1 \overline{\mathbf{V}} \sigma_{jk} \tag{43}$$

for 2D problems.

Eq. (41) is fully defined after computing the sensitivity of the Cauchy stresses vector with respect to the displacement vector, i.e.,  $\partial \sigma_{ik}/\partial \mathbf{u}$ . Using the definition of  $\sigma_{ik}$  from Eq. (14) and the chain rule, we obtain:

$$\frac{\partial \sigma_{jk}}{\partial \mathbf{u}} = \mathbf{D}_{0i} \mathbf{B}_{\ell}. \tag{44}$$

Finally, the sensitivity of the unified yield function with respect to the stress invariants is obtained from Eqs. (8)-(9) and are given by

$$\begin{cases} \frac{\partial A_{jk}}{\partial I_1} = \frac{\partial \sigma_{jk}^{eq}}{\partial I_1} = \hat{\beta} + 2\hat{\gamma}I_1 \\ \frac{\partial A_{jk}}{\partial J_2} = \frac{\partial \sigma_{jk}^{eq}}{\partial I_2} = \frac{\partial \hat{\alpha}(\theta)}{\partial \theta} \frac{\partial \theta}{\partial J_2} \sqrt{3J_2} + \frac{3\hat{\alpha}(\theta)}{2\sqrt{3J_2}} \\ \frac{\partial A_{jk}}{\partial J_3} = \frac{\partial \sigma_{jk}^{eq}}{\partial J_3} = \frac{\partial \hat{\alpha}(\theta)}{\partial \theta} \frac{\partial \theta}{\partial J_3} \sqrt{3J_2}, \end{cases}$$
(45)

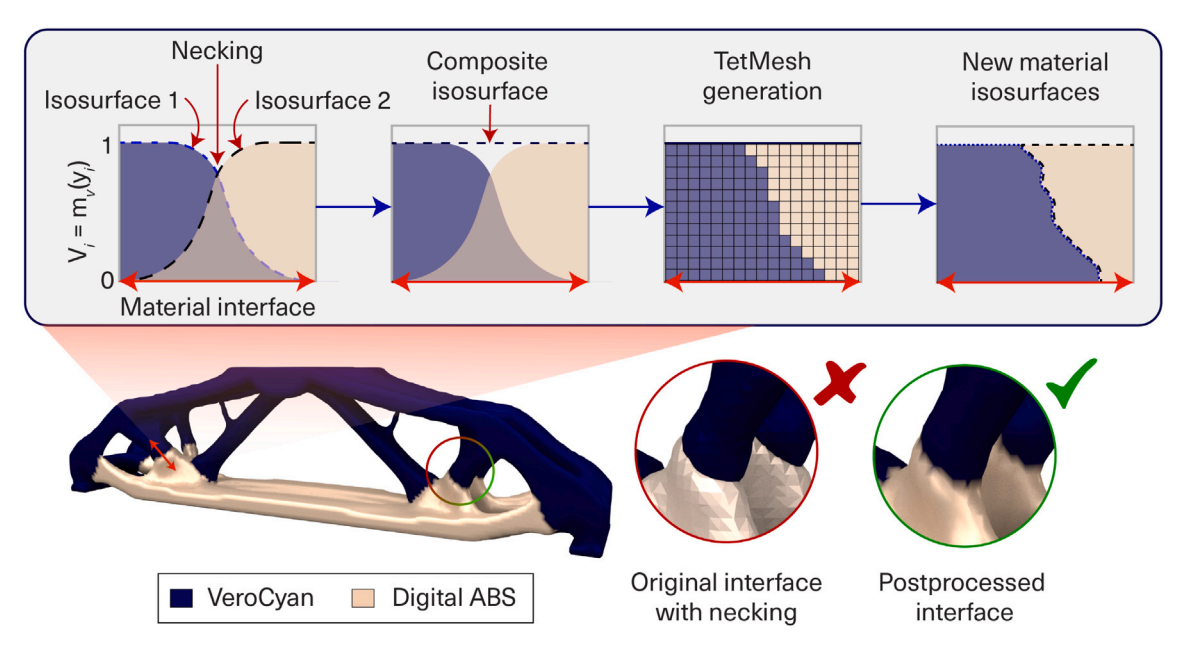


Fig. B.1. Postprocessing routine sequence. First, separate isosurfaces are extracted for each material from the projected density fields, which can produce geometric intersections and necking at the interface (Isosurface 1 and Isosurface 2). A composite density field is then constructed and its isosurface is used to generate a tetrahedral mesh (TetMesh) representing the overall geometry. This mesh is partitioned into material-specific submeshes based on the position of element centroids relative to each material isosurface, producing clean, non-overlapping boundaries. The final material isosurfaces eliminate necking artifacts and are ready for fabrication. The bottom panel shows a beam from Section 5, where the original interface (red inset) exhibits necking, while the postprocessed interface (green inset) is smooth and continuous.

where the partial derivatives of  $\partial \hat{a}(\theta)/\partial \theta$ ,  $\partial \theta/\partial J_2$  and  $\partial \theta/\partial J_3$  can be obtained explicitly from Eqs. (15)–(19).

#### A.1. Sensitivity analysis for multiple load cases

The AL sub-problem (27) can be extended to multiple load cases as follows:

$$J(\mathbf{z}, \mathbf{u}) = f(\mathbf{z}) + \frac{1}{mnN} P(\mathbf{z}, \mathbf{u}),$$
(46)

where n denotes the number of load cases, and the penalty term is given by

$$P = \sum_{c=1}^{n} \sum_{k=1}^{m} \sum_{\ell=1}^{N} \left[ \lambda_{\ell k}^{(c)} h_{\ell k}^{(c)} \left( \mathbf{z}, \mathbf{u}_{c} \right) + \frac{\mu}{2} h_{\ell k}^{(c)^{2}} \left( \mathbf{z}, \mathbf{u}_{c} \right) \right]. \tag{47}$$

The previously derived sensitivities from (31) and (32) remain valid for the multiple-load case problem. However, as in the single-load case, we follow an adjoint sensitivity analysis procedure and reformulate the corresponding sensitivity with respect to  $E_{\ell i}$  as follows:

$$\frac{\partial P}{\partial E_{\ell i}} = \sum_{c=1}^{n} \left[ \sum_{k=1}^{m} \sum_{j=1}^{N} \left[ \lambda_{jk}^{(c)} + \mu h_{jk}^{(c)} \left( \mathbf{z}, \mathbf{u}_{c} \right) \right] \left( \frac{\partial h_{jk}^{(c)} \left( \mathbf{z}, \mathbf{u}_{c} \right)}{\partial E_{\ell i}} + \frac{\partial h_{jk}^{(c)} \left( \mathbf{z}, \mathbf{u}_{c} \right)}{\partial \mathbf{u}_{c}} \cdot \frac{\partial \mathbf{u}_{c}}{\partial E_{\ell i}} \right) \right] 
+ \xi_{c}^{T} \left( \mathbf{K} \frac{\partial \mathbf{u}_{c}}{\partial E_{\ell i}} + \frac{\partial \mathbf{K}}{\partial E_{\ell i}} \mathbf{u}_{c} \right) ,$$
(48)

where  $\mathbf{u}_c$  is the displacement vector associated with load case c, obtained from the equilibrium equation  $\mathbf{K}\mathbf{u}_c = \mathbf{F}_c$ . As for the single-load case, we group all terms involving  $\partial \mathbf{u}_c / \partial E_{\ell i}$  which results in:

$$\frac{\partial P}{\partial E_{\ell i}} = \sum_{c=1}^{n} \sum_{k=1}^{m} \sum_{j=1}^{N} \left[ \lambda_{jk}^{(c)} + \mu h_{jk}^{(c)}(\mathbf{z}, \mathbf{u}_{c}) \right] \frac{\partial h_{jk}^{(c)}(\mathbf{z}, \mathbf{u}_{c})}{\partial E_{\ell i}} + \left( \sum_{c=1}^{n} \sum_{k=1}^{m} \sum_{j=1}^{N} \left[ \lambda_{jk}^{(c)} + \mu h_{jk}^{(c)}(\mathbf{z}, \mathbf{u}_{c}) \right] \frac{\partial h_{jk}^{(c)}(\mathbf{z}, \mathbf{u}_{c})}{\partial \mathbf{u}_{c}} + \xi_{c}^{T} \mathbf{K} \right) \frac{\partial \mathbf{u}_{c}}{\partial E_{\ell i}} + \xi_{c}^{T} \mathbf{u}_{c}. \tag{49}$$

To avoid the expensive computation of  $\partial \mathbf{u}_c/\partial E_{\ell i}$ , we choose the corresponding adjoint vectors  $\boldsymbol{\xi}_c$  such that these terms vanish, leading to the following expression:

$$\frac{\partial P}{\partial E_{\ell i}} = \sum_{c=1}^{n} \left[ \sum_{k=1}^{m} \sum_{i=1}^{N} \left[ \lambda_{jk}^{(c)} + \mu h_{jk}^{(c)} \left( \mathbf{z}, \mathbf{u}_{c} \right) \right] \frac{\partial h_{jk}^{(c)} \left( \mathbf{z}, \mathbf{u}_{c} \right)}{\partial E_{\ell i}} + \xi_{c}^{T} \frac{\partial \mathbf{K}}{\partial E_{\ell i}} \mathbf{u}_{c} \right], \quad (50)$$

where  $\xi_c$  solves the adjoint problem:

$$\mathbf{K}\boldsymbol{\xi}_{c} = -\sum_{k=1}^{m} \sum_{j=1}^{N} \left[ \lambda_{jk}^{(c)} + \mu h_{jk}^{(c)} \left( \mathbf{z}, \mathbf{u}_{c} \right) \right] \frac{\partial h_{jk}^{(c)} \left( \mathbf{z}, \mathbf{u}_{c} \right)}{\partial \mathbf{u}_{c}}.$$
 (51)

The remaining partial derivatives in (50) and (51) are computed in the same manner as in the single-load case.

## Appendix B. Postprocessing of multi-material interfaces

In the context of density-based topology optimization, the optimized material distribution is typically interpreted by extracting an isosurface from the optimized density field using a cutoff density (e.g., 0.5). Although this approach works well for single-material problems, it presents issues in multi-material topology optimization. Specifically, when separate isosurfaces are extracted for each candidate material, geometric intersections between neighboring isosurfaces can create narrow necking regions at material interfaces. These necking artifacts result in localized stress concentrations at material interfaces that may compromise the structural performance of the fabricated multi-material designs.

To address this issue, we implemented a postprocessing routine inspired by the strategy suggested by Sanders et al. [78] and illustrated on Fig. B.1a. This postprocessing scheme eliminates necking artifacts by first constructing a composite density field defined as:

$$\bar{V}_{\ell} = \min\left(\sum_{i=1}^{m} V_{\ell i}, 1\right). \tag{52}$$

An isosurface is extracted from the composite density field and used to generate a tetrahedral mesh (TetMesh) using the iso2mesh toolbox [79], which relies on TetGen [80] to represent the overall structure.

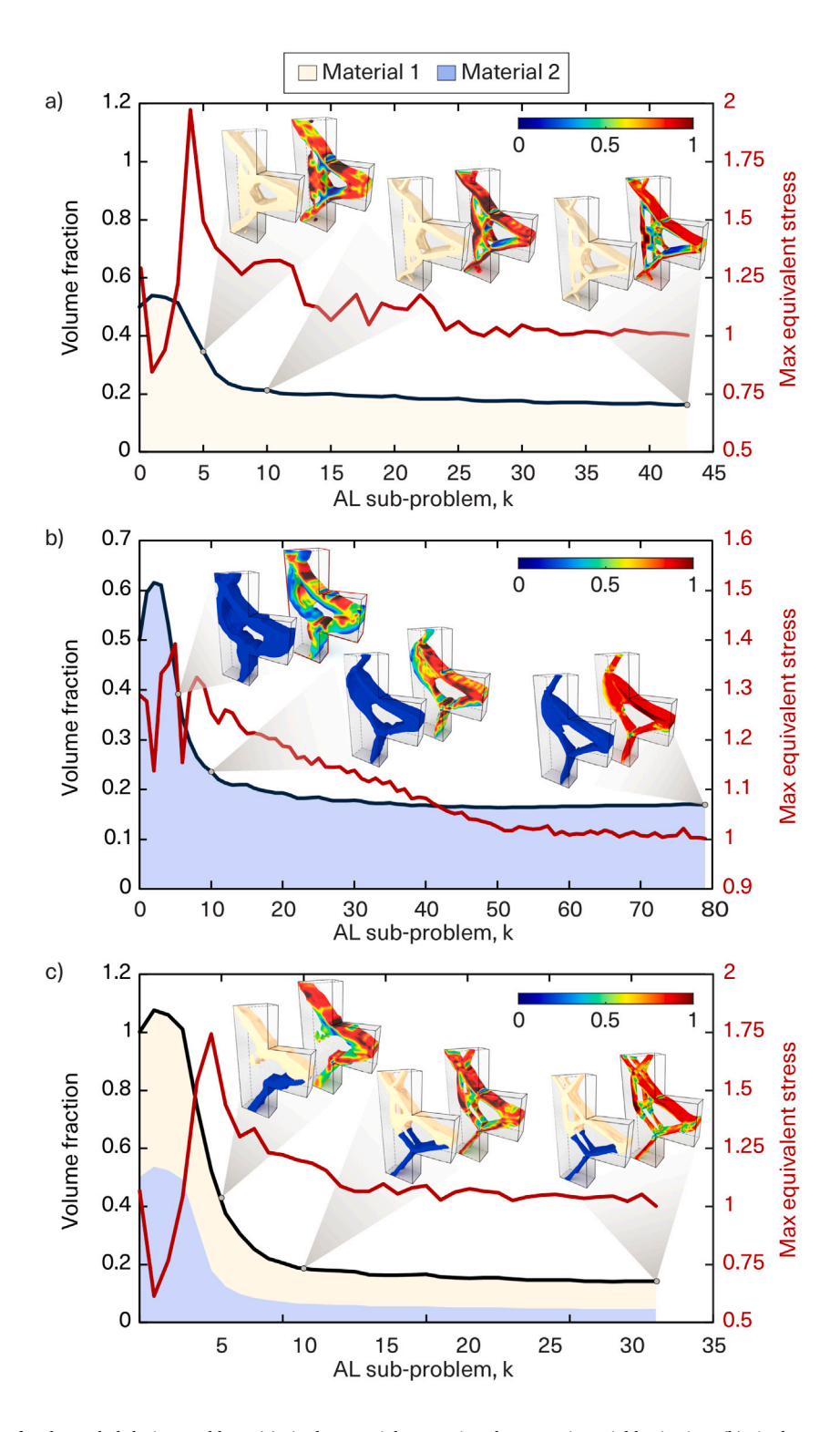
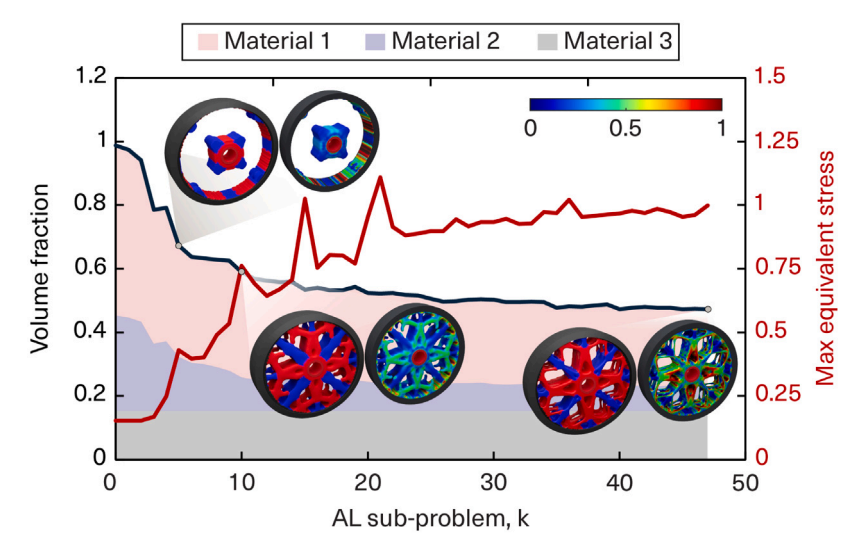


Fig. C.1. Convergence plots for the corbel design problem: (a) single-material case using the von Mises yield criterion, (b) single-material case using the Drucker-Prager yield criterion, and (c) multi-material case. The results are obtained after discretizing one-half of the domain using 314,432 regular hexahedral elements. For each case, the change of volume fraction along the AL iterations, k, is presented in black, while the evolution of the maximum normalized equivalent stress is shown in red. The shaded areas under the volume fraction curve illustrate the contribution of each material to the total volume fraction.



**Fig. C.2.** Convergence plots for the multi-material airless tire problem obtained after discretizing one-half of the domain using 77,200 regular hexahedral elements. The change of volume fraction along the AL iterations, k, is presented in black, while the evolution of the maximum normalized equivalent stress is shown in red. The shaded areas under the volume fraction curve illustrate the contribution of each material to the total volume fraction.

**Table 9**Material properties for the 2D multi-material corbel problem.

Material property	Orange material	Purple material
Weight factor, $\gamma_i$	1	1
Young's modulus, E (GPa)	60	100
Poisson's ratio, v	0.3	0.3
von Mises stress limit, $\sigma_{ m lim}$ (MPa)	90	100

Individual isosurfaces are then generated for each candidate material and used to determine the material phase associated with each tetrahedral element. This is accomplished by checking whether the centroid of an element lies within a given material isosurface. Once identified, the element is tagged with the corresponding material index. In the rare event that an element centroid lies within multiple material isosurfaces, the element is assigned to the first isosurface it intersects, ensuring a unique material assignment for every element.

Once all tetrahedral elements have been assigned a material index, the TetMesh is partitioned into m separate meshes—one per material. The outer surface of each mesh is then identified, resulting in a set of m non-overlapping isosurfaces that are free of necking artifacts. These cleaned isosurfaces are exported as a 3MF file, a format suitable for multi-material additive manufacturing.

This postprocessing procedure effectively eliminates interface necking artifacts caused by intersecting isosurfaces and mitigates the associated stress concentrations. Fig. B.1b illustrates the improvement achieved using our postprocessing routine. The red inset, located to the right of the beam topology, highlights a necked interface obtained using the conventional multi-isosurface approach, while the green inset shows the same region after applying our postprocessing routine.

#### Appendix C. Convergence plots for selected problems

This section summarizes the convergence behavior of all problems discussed in this manuscript. The convergence plots track how the volume fraction, VF, and the maximum equivalent stress,  $\max(\tilde{\sigma}_{\ell i}^{eq}) = \max(E_{\ell i}\sigma_{\ell i}^{eq})$ , evolve at the end of each AL subproblem, k. Fig. C.1 shows the convergence curves for the three corbel designs reported in Section 4.1. Figs. C.1a and C.1b show the results for the single-material designs based on the von Mises and Drucker–Prager yield criteria, respectively, while Fig. C.1c shows the convergence behavior of the two-material design.

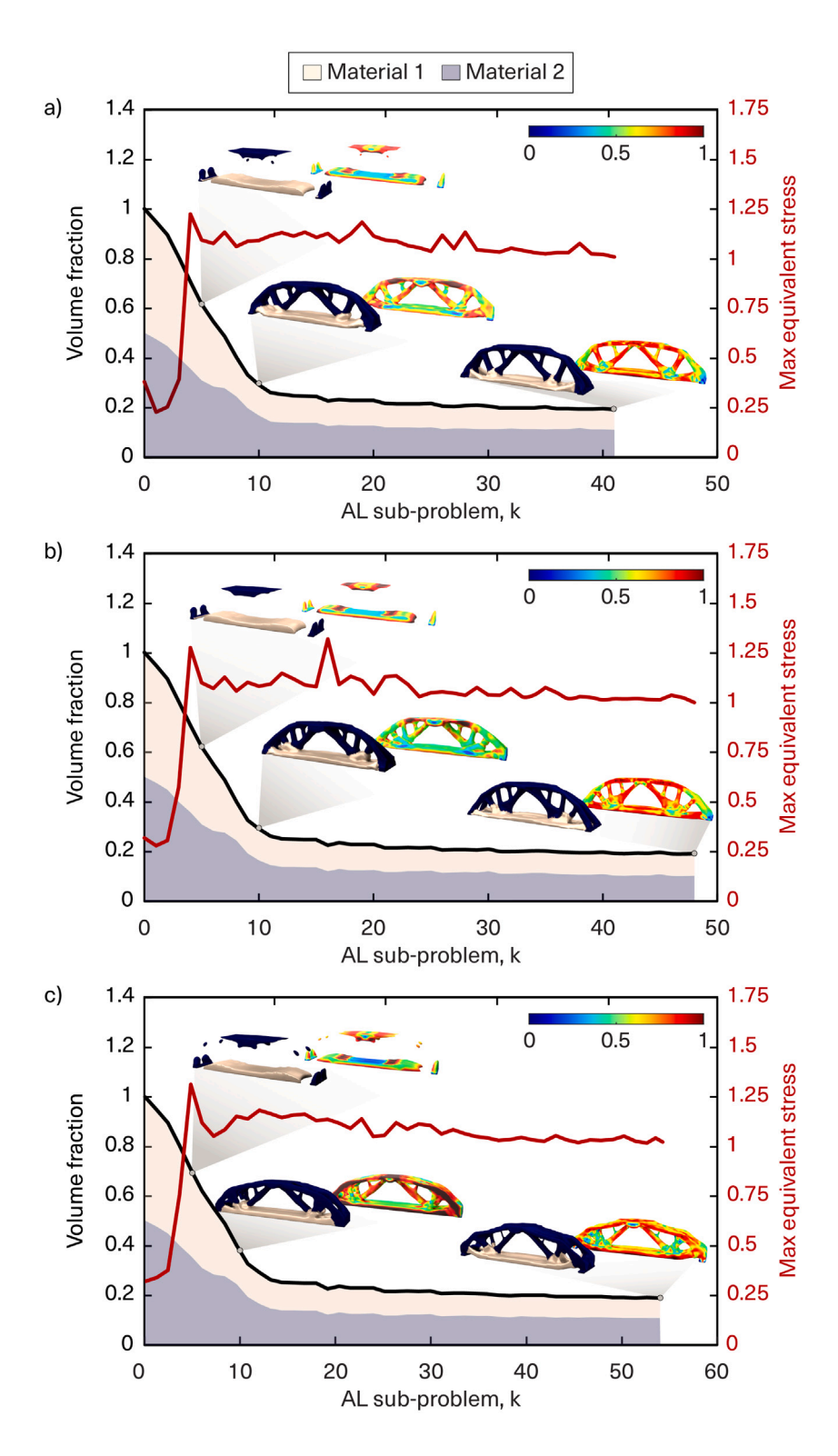
In all three cases, the design domain initially contains 50% of the material density at each element (i.e.,  $z_{\ell i} = 0.5$ ,  $\ell = 1, \ldots, N$  and  $i = 1, \ldots, m$ ). For the two-material design shown in Fig. C.1c, this initialization produces a total volume fraction of 100% due to the overlap of the two candidate materials. During the initial iterations, the volume fraction increases slightly before gradually decreasing as the AL iterations proceed. The designs eventually converge to volume fractions of 16.3%, 17.4%, and 14.0% for the single-material von Mises, the single-material Drucker-Prager, and the two-material cases, respectively. A consistent trend also appears in the evolution of the maximum equivalent stress. During the initial iterations, the maximum equivalent stress decreases as the volume fraction increases, and then reaches a peak once the volume fraction starts to decrease. After this peak, the maximum equivalent stress oscillates with a progressively smaller amplitude until it stabilizes at the limiting value of 1.

Fig. C.2 presents the convergence plot for the multi-material airless tire design discussed in Section 4.2. Unlike the results discussed before, here the maximum equivalent stress remains below the prescribed limit throughout the optimization iterations. Convergence is achieved as the volume fraction decreases and the maximum equivalent stress reaches the maximum allowable value of 1.

Fig. C.3 presents the convergence plot for the multi-material beam discussed in Section 5, which considered three different yield criteria, namely Drucker–Prager, Willam–Warnke, and Mohr–Coulomb. In this problem, the volume fraction consistently decreases throughout the AL iterations for all three design cases. Meanwhile, the maximum equivalent stress exhibits a rapid increase during the initial iterations, followed by oscillations above the allowable limit of 1 until convergence is achieved.

## Appendix D. Sensitivity to algorithmic parameters

This appendix investigates the sensitivity of the proposed framework to key algorithmic parameters that influence the quality of the



**Fig. C.3.** Convergence plots for the multi-material beam problem: (a) results using the Drucker–Prager yield criterion, (b) results using the Willam–Warnke yield criterion, and (c) results using the Mohr–Coulomb yield criterion. The results are obtained after discretizing one-half of the domain using 98,784 regular hexahedral elements. For each case, the change of volume fraction along the AL iterations, k, is presented in black, while the evolution of the maximum equivalent stress is shown in red. The shaded areas under the volume fraction curve illustrate the contribution of each material to the total volume fraction.

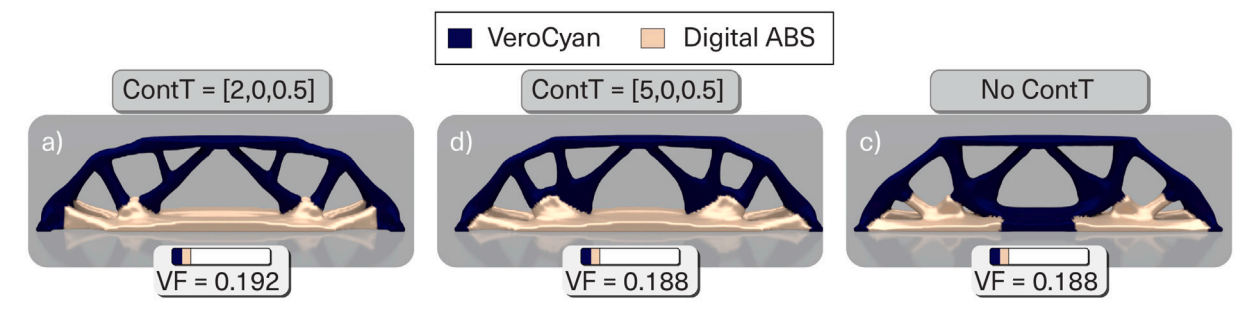


**Fig. D.1.** Effect of the mixing penalty term on the final topology for the Drucker–Prager beam. (a) Continuation scheme with  $\tau$  initialized at 0 and increased by 0.5 every two AL iterations until reaching  $\tau = 1$ . (b) Continuation scheme with  $\tau$  initialized at 0 and increased by 0.5 every five AL iterations until reaching  $\tau = 1$ . (c) No continuation scheme, with  $\tau = 1$  applied from the beginning of the optimization.

optimized designs. While the results discussed previously focused on demonstrating the overall capabilities of our AL-based framework, here we provide a more detailed examination of how parameter choices affect the optimization results. We first study the effects of continuation of the mixing penalty term  $\tau$  used in the DMO interpolation function, and then examine the influence of the cutoff density  $\bar{\eta}$  and projection sharpness  $\bar{\beta}$  in the threshold projection of the design variables.

#### D.1. Influence of the continuation on the mixing penalty term

Fig. D.1 examines how different continuation strategies for the mixing penalty term,  $\tau$ , affect the optimized beam designs discussed in Section 5.3. For illustration purposes, we focus on the beam designed using the Drucker–Prager yield criterion. Here, we compare three strategies: (a) the baseline scheme from Section 5.3, where  $\tau$  starts at 0 and increases by 0.5 every two AL iterations until reaching a value of 1; (b) a slower continuation using the same 0.5 increments, but this time applied every five AL iterations; and (c) no continuation, where  $\tau=1$  is enforced from the start.

A comparison between Figs. D.1a-b shows that the rate at which  $\tau$ increases affects the final design. Nevertheless, the overall topological features remain qualitatively similar between these two designs, with the resulting volume fractions differing by only 2%. In contrast, enforcing  $\tau = 1$  from the start (Fig. D.1c) produces a noticeably different material distribution, wherein the tension-dominated region along the bottom chord contains a combination of VeroCyan and Digital ABS), unlike the other two designs where this region is composed solely of Digital ABS. Despite producing a different topology, the optimized volume fraction for case (c) is almost identical to that for case (b). These differences in optimized designs are expected in highly nonlinear and non-convex problems such as the stress-constrained topology optimization problem introduced here, where even small changes in input parameters (e.g., those related to the DMO interpolation function) can steer the optimizer toward a different local minimum. Based on these observations, we adopted the parameter set from Fig. D.1a for the results presented in Section 5.3, as it produced the most consistent designs across the yield criteria studied.

## D.2. Influence of the threshold projection parameters

Here we investigate the influence of the cutoff density  $\bar{\eta}$  and the projection sharpness  $\bar{\beta}$  in Eq. (2) on the optimized topologies of a 2D corbel problem previously studied by Kundu et al. [53]. The problem considers two candidate materials with properties summarized in Table 9. Consistently with [53], the results we discuss next are obtained for a design domain discretized into 40,000 regular quadrilateral elements, and using a filter radius of R=0.19 m.

Fig. D.2 illustrates the topologies obtained after solving the first 10 AL subproblems. We selected to display the results at this stage because variations in  $\bar{\eta}$  and  $\bar{\beta}$  have the most pronounced effect on topology

during the early stages of the optimization process. In Fig. D.2a, the cutoff density is fixed at  $\bar{\eta}=0.5$ , while the projection sharpness takes values of  $\bar{\beta}=1$ ,  $\bar{\beta}=5$ , or  $\bar{\beta}=10$ . When  $\bar{\beta}=1$ , the topology exhibits blurred boundaries and an increased volume fraction due to the intermediate densities along the edges. Increasing  $\bar{\beta}$  to 5 reduces these diffuse regions and sharpens the boundaries, although some blurring persists. A further increase to  $\bar{\beta}=10$  introduces stronger nonlinearity, steering the optimizer toward a different local minimum with a lower volume fraction and more small-scale features.

Fig. D.2b explores the effect of varying the cutoff density  $\bar{\eta}$  while keeping the projection sharpness fixed at  $\bar{\beta}=5$ . For this study, we consider three cutoff values:  $\bar{\eta}=0.4,\ \bar{\eta}=0.5,\$ and  $\bar{\eta}=0.6.$  The results demonstrate a strong sensitivity to  $\bar{\eta}$ , as each case converges to a different topology. Similarly to previous discussions, this behavior reflects the highly nonlinear and non-convex nature of the optimization problem, where even small changes in input parameters can lead the optimizer to different local minima. Lower cutoff values ( $\bar{\eta}=0.4$ ) promote more compact designs, possibly due to the early removal of understressed regions, whereas higher cutoff values ( $\bar{\eta}=0.6$ ) allow material to be distributed further from the corners, producing a finer and more distributed layout.

## Appendix E. Nomenclature

$E_{\ell i}$	Penalized densities for element $\ell$ and
	candidate material <i>i</i> using the SIMP
	interpolation function
$I_1$	First invariant of the Cauchy stress tensor
$J_2$	Second invariant of the Cauchy stress tensor
$J_3$	Third invariant of the Cauchy stress tensor
$N_c$	Total number of stress constraints
$P(\mathbf{z}, \mathbf{u})$	Penalization term in the AL function
R	Filter radius
$W_{\ell i}$	Stiffness interpolation function
$J^{(k)}$	Augmented Lagrangian function at the kth
	sub-problem
VF	Multi-material volume fraction
N	Number of elements in the finite element
	mesh
$f(\mathbf{z})$	Objective function
$g_{\ell i}(\mathbf{z}, \mathbf{u})$	Stress constraint of element $\ell$ and material $i$
$h_{\ell i}\left(\mathbf{z},\mathbf{u}\right)$	Modified stress constraint of element $\ell$ and
	material <i>i</i> for the AL method with inequality
	constraints
n	Number of load cases
p	SIMP penalization parameter
q	Nonlinear filter exponent
m	Number of candidate materials
$\Lambda_{\ell i}$	Unified yield function

 $\mathbf{V}_{i}$ 

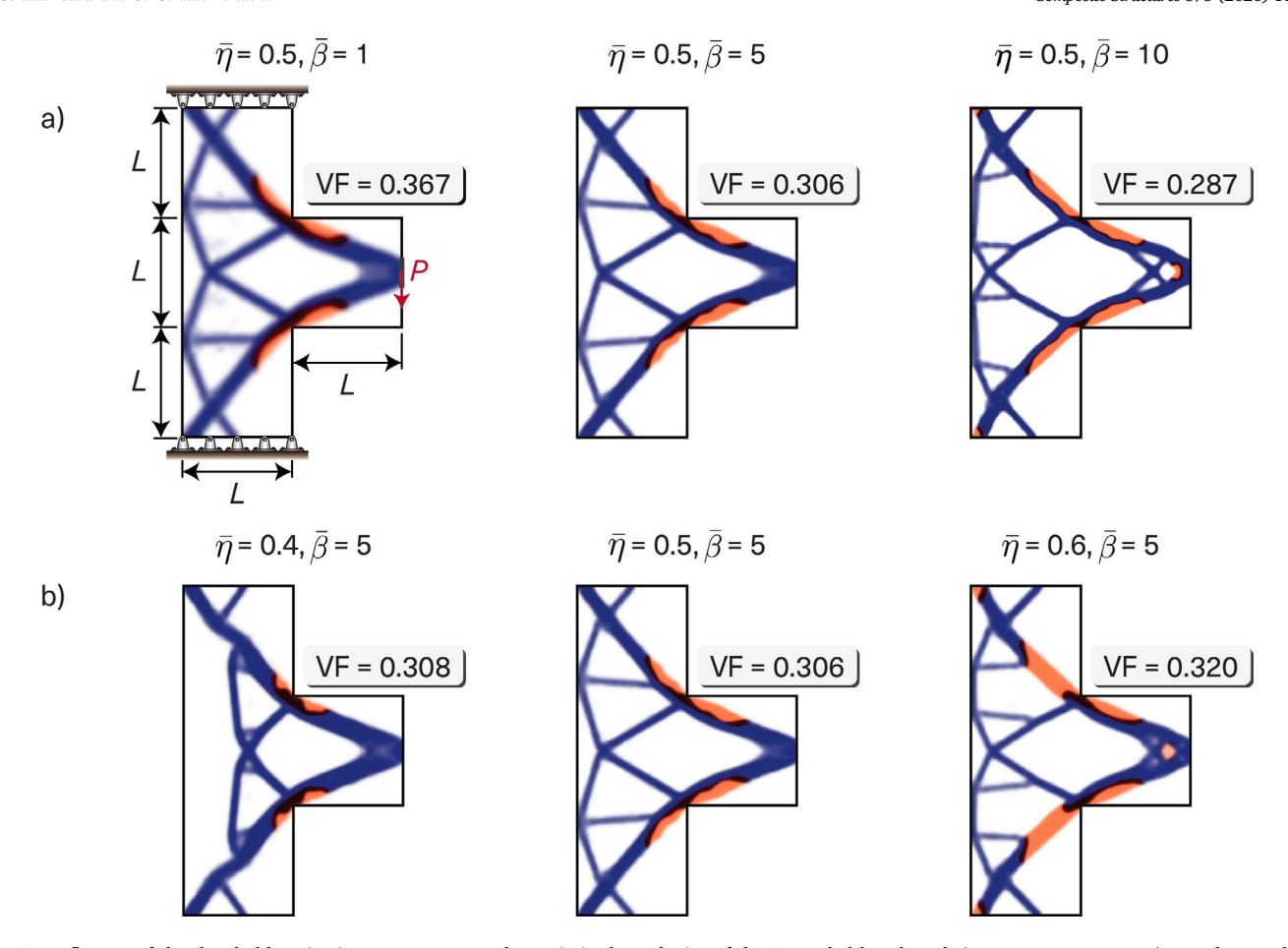


Fig. D.2. Influence of the threshold projection parameters on the optimized topologies of the 2D corbel benchmark (L=2 m, P=21.2 MN). Results are shown after the first 10 AL subproblems. (a) Fixed cutoff density  $\bar{\eta}=0.5$  with three projection sharpness values:  $\bar{\beta}=1,5,10$ . (b) Fixed projection sharpness  $\bar{\beta}=5$  with three cutoff densities:  $\bar{\eta}=0.4,0.5,0.6$ .

$ar{eta}$	Parameter used to control the aggressiveness	$\mathbf{F}_c$	Force vector associated with load case $c$
	of the threshold projection function	A	Vector of element area (in 2D) or volume
$ar{\eta}$	Threshold density cutoff value		(in 3D) of each finite element
$\gamma_i$	Weight factor associated with candidate	$\overline{\mathbf{M}}$	Vector used to evaluate the first invariant of
	material i		the Cauchy stress tensor
$\hat{lpha}$	Deviatoric component of the unified yield	$\overline{\mathbf{v}}$	Matrix used to evaluate the second invariant
	function		of the Cauchy stress tensor
$\hat{eta}$	Unified yield function parameter	F	Global force vector
γ̂	Unified yield function parameter	K	Global stiffness matrix
$\hat{ heta}$	Modified Lode angle	P	Filter matrix
$\mu^{(k)}$	Penalty parameter at the kth iteration of the	$\mathbf{k}_{\mathscr{C}}$	Local stiffness matrix of element $\ell$
	AL method	$\mathbf{u}_{\ell}$	Displacement vector of element $\ell$
$\sigma^{eq}_{\ell i}$	Equivalent stress measure at the centroid of	z	Matrix of design variables
	element $\ell$ for material $i$	$\mathbf{u}_c$	Displacement vector associated with load
$\sigma_{ m lim}$	von Mises yield stress	·	case c
$\sigma_b$	Yield stress in equibiaxial compression	$\mathbf{y}_i$	Vector of filtered densities
$\sigma_c$	Yield stress in uniaxial compression	u	Global displacement vector
$\sigma_t$	Yield stress in uniaxial tension	$\lambda_{m{j}}^{(k)}$	Vector of approximated Lagrange multipliers
$\theta$	Lode angle	J	at the <i>k</i> th iteration of the AL method
$ ilde{lpha}$	Parameter to update the penalty parameter	$\boldsymbol{\xi}_c$	Adjoint vector associated with load case <i>c</i>
	$\mu^{(k)}$	J.C	used for sensitivity evaluation
$ ilde{\sigma}^{eq}_{\ell i}$	Normalized equivalent stress measure	$\sigma_{\ell i}$	Vector of Cauchy stress values for material <i>i</i>
$\mathbf{B}_{\ell}$	Strain displacement matrix at the centroid	v i	at the centroid of element $\ell$
	of element $\ell$		
$\mathbf{D}_{0i}$	Material moduli matrix of the solid material	Data availability	

Vector of element volume fractions for

material i

Data will be made available upon request.

#### References

- [1] Giraldo-Londoño O, Paulino GH. A unified approach for topology optimization with local stress constraints considering various failure criteria: von Mises, Drucker-Prager, Tresca, Mohr-Coulomb, Bresler-Pister and Willam-Warnke. Proc B Soc A 2020:476(2238):20190861.
- [2] Giraldo-Londoño O, Paulino GH. PolyStress: a Matlab implementation for local stress-constrained topology optimization using the augmented Lagrangian method. Struct Multidiscip Optim 2021;63(4):2065–97.
- [3] Giraldo-Londoño O, Russ JB, Aguiló MA, Paulino GH. Limiting the first principal stress in topology optimization: a local and consistent approach. Struct Multidiscip Optim 2022;65(9):254.
- [4] Bendsøe MP, Kikuchi N. Generating optimal topologies in structural design using a homogenization method. Comput Methods Appl Mech Engrg 1988;71(2):197–224.
- [5] Gaynor AT, Meisel NA, Williams CB, Guest JK. Multiple-material topology optimization of compliant mechanisms created via PolyJet three-dimensional printing. J Manuf Sci Eng 2014;136(6):061015.
- [6] Takezawa A, Kobashi M. Design methodology for porous composites with tunable thermal expansion produced by multi-material topology optimization and additive manufacturing. Compos Part B: Eng 2017;131:21–9.
- [7] Gibiansky LV, Sigmund O. Multiphase composites with extremal bulk modulus. J Mech Phys Solids 2000;48(3):461–98.
- [8] Zhang XS, Paulino GH, Ramos AS. Multi-material topology optimization with multiple volume constraints: a general approach applied to ground structures with material nonlinearity. Struct Multidiscip Optim 2018;57:161–82.
- [9] Taheri AH, Hassani B. Simultaneous isogeometrical shape and material design of functionally graded structures for optimal eigenfrequencies. Comput Methods Appl Mech Engrg 2014;277:46–80.
- [10] Sved G, Ginos Z. Structural optimization under multiple loading. Int J Mech Sci 1968;10(10):803–5.
- [11] Duysinx P, Bendsøe MP. Topology optimization of continuum structures with local stress constraints. Internat J Numer Methods Engrg 1998;43(8):1453–78.
- [12] Thomsen J. Topology optimization of structures composed of one or two materials. Struct Optim 1992;5:108–15.
- [13] Bendsøe MP. Optimal shape design as a material distribution problem. Struct Optim 1989;1:193–202.
- [14] Zhou M, Rozvany GI. The COC algorithm, part II: Topological, geometrical and generalized shape optimization. Comput Methods Appl Mech Engrg 1991:89(1-3):309-36.
- [15] Bendsøe MP, Sigmund O. Material interpolation schemes in topology optimization. Arch Appl Mech 1999;69:635–54.
- [16] Stegmann J, Lund E. Discrete material optimization of general composite shell structures. Internat J Numer Methods Engrg 2005;62(14):2009–27.
- [17] Lund E, Stegmann J. On structural optimization of composite shell structures using a discrete constitutive parametrization. Wind Energy 2005;8(1):109–24.
- [18] Sanders ED, Pereira A, Aguiló MA, Paulino GH. PolyMat: an efficient Matlab code for multi-material topology optimization. Struct Multidiscip Optim 2018;58:2727–59.
- [19] Giraldo-Londoño O, Paulino GH. Fractional topology optimization of periodic multi-material viscoelastic microstructures with tailored energy dissipation. Comput Methods Appl Mech Engrg 2020;372:113307.
- [20] Giraldo-Londoño O, Mirabella L, Dalloro L, Paulino GH. Multi-material thermomechanical topology optimization with applications to additive manufacturing: Design of main composite part and its support structure. Comput Methods Appl Mech Engrg 2020;363:112812.
- [21] Yang R, Chen C. Stress-based topology optimization. Struct Optim 1996;12:98–105.
- [22] Duysinx P, Sigmund O. New developments in handling stress constraints in optimal material distribution. In: 7th AIAA/USAf/NASA/ISSMO symposium on multidisciplinary analysis and optimization. 1998, p. 4906.
- [23] Lee E, James KA, Martins JR. Stress-constrained topology optimization with design-dependent loading. Struct Multidiscip Optim 2012;46:647–61.
- [24] Xia Q, Shi T, Liu S, Wang MY. A level set solution to the stress-based structural shape and topology optimization. Comput Struct 2012;90:55–64.
- [25] Lian H, Christiansen AN, Tortorelli DA, Sigmund O, Aage N. Combined shape and topology optimization for minimization of maximal von Mises stress. Struct Multidiscip Optim 2017;55:1541–57.
- [26] Sharma A, Maute K. Stress-based topology optimization using spatial gradient stabilized XFEM. Struct Multidiscip Optim 2018;57:17–38.
- [27] Kreisselmeier G, Steinhauser R. Systematic control design by optimizing a vector performance index. In: Computer aided design of control systems. Elsevier; 1980, p. 113–7
- [28] Park YK. Extensions of optimal layout design using the homogenization method. [Ph.D. thesis], Ann Arbor: University of Michigan; 1995.
- [29] Le C, Norato J, Bruns T, Ha C, Tortorelli D. Stress-based topology optimization for continua. Struct Multidiscip Optim 2010;41:605–20.
- [30] Holmberg E, Torstenfelt B, Klarbring A. Stress constrained topology optimization. Struct Multidiscip Optim 2013;48:33–47.

- [31] París J, Navarrina F, Colominas I, Casteleiro M. Block aggregation of stress constraints in topology optimization of structures. Adv Eng Softw 2010;41(3):433–41.
- [32] Bertsekas DP. Nonlinear programming. Cambridge, MA, USA: MIT Press; 1999.
- [33] Nocedal J, Wright SJ. Numerical optimization. 2nd ed. Berlin: Springer; 2006.
- [34] Bertsekas DP. Constrained optimization and Lagrange multiplier methods. New York, London: Academic Press; 1982.
- [35] Izmailov AF, Solodov MV, Uskov E. Global convergence of augmented Lagrangian methods applied to optimization problems with degenerate constraints, including problems with complementarity constraints. SIAM J Optim 2012;22(4):1579–606.
- [36] Andreani R, Haeser G, Schuverdt ML, Silva PJ. A relaxed constant positive linear dependence constraint qualification and applications. Math Program 2012;135(1):255–73.
- [37] Pereira JT, Fancello EA, Barcellos CS. Topology optimization of continuum structures with material failure constraints. Struct Multidiscip Optim 2004;26:50–66.
- [38] Emmendoerfer Jr. H, Fancello EA. A level set approach for topology optimization with local stress constraints. Internat J Numer Methods Engrg 2014;99(2):129–56.
- [39] Emmendoerfer Jr. H, Fancello EA. Topology optimization with local stress constraint based on level set evolution via reaction-diffusion. Comput Methods Appl Mech Engrg 2016;305:62–88.
- [40] Senhora FV, Giraldo-Londoño O, Menezes IFM, Paulino GH. Topology optimization with local stress constraints: A stress aggregation-free approach. Struct Multidiscip Optim 2020;62:1639–68.
- [41] Da Silva G, Beck AT, Cardoso EL. Topology optimization of continuum structures with stress constraints and uncertainties in loading. Internat J Numer Methods Engrg 2018;113(1):153–78.
- [42] Giraldo-Londoño O, Aguiló MA, Paulino GH. Local stress constraints in topology optimization of structures subjected to arbitrary dynamic loads: a stress aggregation-free approach. Struct Multidiscip Optim 2021;64:3287–309.
- [43] Kirsch U. On singular topologies in optimum structural design. Struct Optim 1990;2:133–42.
- [44] Cheng GD, Guo X. ε-Relaxed approach in structural topology optimization. Struct Optim 1997:13:258–66.
- [45] Bruggi M, Duysinx P. Topology optimization for minimum weight with compliance and stress constraints. Struct Multidiscip Optim 2012;46:369–84.
- [46] Cheng G, Jiang Z. Study on topology optimization with stress constraints. Eng Optim 1992;20(2):129–48.
- [47] Jeong SH, Choi D-H, Yoon GH. Separable stress interpolation scheme for stress-based topology optimization with multiple homogenous materials. Finite Elem Anal Des 2014;82:16–31.
- [48] Chu S, Xiao M, Gao L, Li H. A level set-based method for stress-constrained multimaterial topology optimization of minimizing a global measure of stress. Internat J Numer Methods Engrg 2019;117(7):800–18.
- [49] Xu S, Liu J, Zou B, Li Q, Ma Y. Stress constrained multi-material topology optimization with the ordered SIMP method. Comput Methods Appl Mech Engrg 2021;373:113453.
- [50] Han Z, Wei K, Gu Z, Ma X, Yang X. Stress-constrained multi-material topology optimization via an improved alternating active-phase algorithm. Eng Optim 2022;54(2):305–28.
- [51] Huang X, Chen Y, Hou L, Miao C, Li Y. Stress-related multi-material structures topology optimization with gradient interfaces. Compos Struct 2025;119176.
- [52] Chen J, Zhao Q, Zhang L. Multi-material topology optimization of thermo-elastic structures with stress constraint. Mathematics 2022;10(8):1216.
- [53] Kundu RD, Li W, Zhang XS. Multimaterial stress-constrained topology optimization with multiple distinct yield criteria. Extrem Mech Lett 2022;54:101716.
- [54] Ding W, Liao H, Yuan X. Multi-material topology optimization considering arbitrary strength and yield criteria constraints with single-variable interpolation. Internat J Numer Methods Engrg 2024;125(19):e7561.
- [55] Chu S, Gao L, Xiao M, Luo Z, Li H. Stress-based multi-material topology optimization of compliant mechanisms. Internat J Numer Methods Engrg 2018;113(7):1021–44.
- [56] Liao H, Ding W, Ai S, Gao R. A single variable stress-based multi-material topology optimization method with three-dimensional unstructured meshes. Comput Methods Appl Mech Engrg 2024;421:116774.
- [57] Yaghoobi A, Asghari M, Babaei H. Introducing material-specific stress constraints in multi-material topology optimization. Comput Struct 2025;313:107756.
- [58] Kundu RD, Zhang XS. Additive manufacturing of stiff and strong structures by leveraging printing-induced strength anisotropy in topology optimization. Addit Manuf 2023;75:103730.
- [59] Kundu RD, Zhang XS. Sustainability-oriented multimaterial topology optimization: designing efficient structures incorporating environmental effects. Struct Multidiscip Optim 2025;68(1):17.
- [60] Wang F, Lazarov BS, Sigmund O. On projection methods, convergence and robust formulations in topology optimization. Struct Multidiscip Optim 2011;43:767–84.
- [61] Zegard T, Paulino GH. Bridging topology optimization and additive manufacturing. Struct Multidiscip Optim 2016;53:175–92.

- [62] Lode W. Versuche über den Einfluß der mittleren Hauptspannung auf das Fließ en der Metalle Eisen, Kupfer und Nickel. Z Phys 1926;36(11):913–39.
- [63] Abbo A, Sloan S. A smooth hyperbolic approximation to the Mohr-Coulomb yield criterion. Comput Struct 1995;54(3):427–41.
- [64] Libonati F, Gu GX, Qin Z, Vergani L, Buehler MJ. Bone-inspired materials by design: toughness amplification observed using 3D printing and testing. Adv Eng Mater 2016;18(8):1354–63.
- [65] Zorzetto L, Andena L, Briatico-Vangosa F, De Noni L, Thomassin J-M, Jérôme C, Grossman Q, Mertens A, Weinkamer R, Rink M, et al. Properties and role of interfaces in multimaterial 3D printed composites. Sci Rep 2020;10(1):22285.
- [66] Svanberg K. The method of moving asymptotes-a new method for structural optimization. Internat J Numer Methods Engrg 1987;24(2):359–73.
- [67] Mueller J, Courty D, Spielhofer M, Spolenak R, Shea K. Mechanical properties of interfaces in inkjet 3D printed single-and multi-material parts. 3D Print Addit Manuf 2017;4(4):193–9.
- [68] Stratasys. PolyJet technology for 3D printing | Stratasys stratasys.com. 2015, https://www.stratasys.com/en/guide-to-3d-printing/technologies-and-materials/polyjet-technology/. [Accessed 09 March 2025].
- [69] ASTM. D695: Standard test method for compressive properties of rigid plastics. 2023.
- [70] ASTM. D638: Standard test method for tensile properties of plastics. 2022.
- [71] Cazón A, Morer P, Matey L. PolyJet technology for product prototyping: Tensile strength and surface roughness properties. Proc Inst Mech Eng Part B: J Eng Manuf 2014;228(12):1664–75.

- [72] Zohdi N, Yang R. Material anisotropy in additively manufactured polymers and polymer composites: a review. Polymers 2021;13(19):3368.
- [73] Štaffová M, Ondreáš F, Svatík J, Zbončák M, Jančář J, Lepcio P. 3D printing and post-curing optimization of photopolymerized structures: Basic concepts and effective tools for improved thermomechanical properties. Polym Test 2022:108:107499.
- [74] Yap T, He Z, Wang Z, Tamijani A, Tehrani M. Experimental investigation and validation of strength-based topology and fiber path optimization in additively manufactured continuous fiber reinforced composites. Addit Manuf 2024;89:104274.
- [75] Tsai SW, Wu EM. A general theory of strength for anisotropic materials. J Compos Mater 1971;5(1):58–80.
- [76] Liu C, Huang Y, Stout M. On the asymmetric yield surface of plastically orthotropic materials: a phenomenological study. Acta Mater 1997;45(6):2397–406.
- [77] Giraldo-Londoño O, Paulino GH. PolyDyna: a Matlab implementation for topology optimization of structures subjected to dynamic loads. Struct Multidiscip Optim 2021;64(2):957–90.
- [78] Sanders E, Pereira A, Paulino G. Optimal and continuous multilattice embedding. Sci Adv 2021;7(16):eabf4838.
- [79] Fang Q, Boas DA. Tetrahedral mesh generation from volumetric binary and grayscale images. In: Proc IEEE Int Symp Biomed Imaging From Nano Macro. IEEE; 2009, p. 1142-5.
- [80] Hang S. TetGen, a Delaunay-based quality tetrahedral mesh generator. ACM Trans Math Software 2015;41(2):11.